Cement and Concrete Composites 148 (2024) 105449

Contents lists available at ScienceDirect

Cement and Concrete Composites

journal homepage: www.elsevier.com/locate/cemconcomp

A comprehensive review of ultra-high performance concrete (UHPC) behaviour under blast loads

Jian Liu [a,b], Jie Wei [a,b], Jun Li [c,**], Yu Su [d], Chengqing Wu [c,*]

[a] Earthquake Engineering Research and Test Center, Guangzhou University, Guangzhou, 510405, China
[b] Key Laboratory of Earthquake Resistance, Earthquake Mitigation and Structural Safety, Ministry of Education, Guangzhou, 510405, China
[c] School of Civil and Environmental Engineering, University of Technology Sydney, Ultimo, NSW, 2007, Australia
[d] Hubei RockTek Limited Company, Daye, 435100, China

ARTICLE INFO

Keywords:
Ultra-high performance concrete (UHPC)
Structural member
UHPC-Based composite structure
Blast load
Dynamic performance

ABSTRACT

Blasts resulted from industrial/residential accidents and deliberate attacks can impose extremely hazardous loading conditions upon nearby structures. The repercussions of these blasts encompass not only direct effects such as blast overpressure and fragments but also indirect outcomes like progressive collapse of structures. In the pursuit of enhanced protection for concrete structures, substantial endeavors have been directed towards developing innovative construction materials with outstanding properties, among which the ultra-high performance concrete (UHPC) has emerged as a notable representative. Drawing from existing experimental, numerical and theoretical studies, this paper presents an inclusive overview of recent progress in UHPC structural members (slabs, beams and columns) and UHPC-based composite structures (mesh reinforced UHPC, UHPC-filled steel tube and UHPC strengthening of normal reinforced concrete (NRC) structures) in their ability to withstand blast loads. While discussing the exceptional material and structural dynamic performance of UHPC, recommendations are offered for the further research directions in utilising UHPC structures to resist blast loads, which include exploring eco-friendly UHPC, integrating 3D printing technology and employing machine learning analytical methods.

1. Introduction

Over the past few decades, there has been a rise in accidental or anthropogenic blast incidents, highlighting the global concern for improving the anti-explosion performance of concrete structures. When exposed to blast loads, concrete structural members can experience a variety of failure modes, involving flexural failure, direct shear failure and concrete spalling. These multiple failure modes may lead to the loss of load-carrying capacity in individual or multiple key structural members, potentially triggering catastrophic consequences such as progressive collapse. The inadequate tensile properties and brittleness of conventional concrete greatly impact the overall structural safety under blast loads. Although incorporating steel reinforcement can partially address these shortcomings to some extent, it remains crucial to adopt advanced concrete materials with exceptional properties to bolster the blast resilience of concrete structures.

Concrete technology has witnessed remarkable advancements over the past few decades and ultra-high performance concrete (UHPC) emerges as a promsing new concrete material. Equipped with exceptional mechanical properties, durability and damage tolerance, UHPC stands out as a premier composite material in both civil and military constructions especially in structural hardening design against impuslive loads. Comprehending the dynamic behaviour of UHPC structures exposed to blast loads is of paramount importance for structural protection and design. This section will briefly introduce the UHPC composition, static and dynamic material properties, characteristics of blast loads, concrete structural response under blast loads, and analysis techniques for UHPC structures under blast loads.

1.1. UHPC composition, preparation, properties and applications

As illustrated in Fig. 1, differing from the composition of conventional concretes like normal strength concrete (NSC) and high strength concrete (HSC), UHPC employs the maximum densified particle packing

* Corresponding author.
** Corresponding author.
E-mail addresses: jun.li-2@uts.edu.au (J. Li), chengqing.wu@uts.edu.au (C. Wu).

https://doi.org/10.1016/j.cemconcomp.2024.105449
Received 6 October 2023; Received in revised form 9 January 2024; Accepted 22 January 2024
Available online 23 January 2024

theory [1]. This theory eliminates the use of coarse aggregates and instead combines particles of varying sizes in optimal proportions to achieve the most tightly packed configuration. The gaps between millimeter-sized particles (fine aggregates) are filled with micrometer-sized particles, such as cement and mineral admixtures, and the gaps formed by micrometer-sized particles are filled with nanoscale reactive powders like silica fume. This contributes to a more compact concrete matrix with enhanced constituent reactivity, thereby having reduced initial microcracks and capillary pores. Owing to the addition of superplasticizer, the water-to-binder ratio in UHPC is largely reduced, typically not exceeding 0.2. To counteract the inherent brittleness of UHPC resulting from the increased material compactness, a large amount of fibres is commonly included. Besides the improved concrete ductility and toughness, the fibre reinforcement can make use of the frictional pull-out capacity to dissipate the imposed energy and provides a bridging effect to inhibit concrete spalling and crack propagation. UHPC is generally cured in 80–90 °C hot water to promote the pozzolanic effect of silica fumes, resulting in higher mechanical strengths and denser microstructures than ambient or water-cured UHPC.

Fig. 2(a) illustrates a comparison of uniaxial compressive and tensile behaviors among different concrete types, including NSC [3], 2 vol-% steel fibre reinforced HSC [4,5] and UHPC [6]. It is evident that UHPC displays enhanced properties involving elastic modulus, uniaxial compressive strength and ductility in comparison to NSC and HSC. Additionally, UHPC exhibits notable strain-softening behavior upon reaching the peak tensile stress, and the manifestation of strain-hardening behaviour in UHPC during tension is significantly influenced by some factors such as fiber type, content, geometry and orientation [7]. Under dynamic loading conditions with typical strain rate intervals relevant to concrete materials [8], as illustrated in Fig. 3, the material propertis of concrete diverge from those ovserved from the quasi-static loading conditions. Typically, the strength, strain capacity and toughness of concrete tend to enhance with the increase in the strain rate [9,10]. The strain rate effect on both compressive and tensile strengths is encapsulated by the dynamic increase factor (DIF), which represents the ratio of dynamic strength to quasi-static strength across a broad range of strain rates. Because of the incorporation of fibres and denser microstructures, UHPC may exhibit distinct strain rate sensitivity when compared to the conventional concrete. Fig. 2(b) presents the compressive and tensile DIF values of UHPC, utilising the empirical models established by Fujikake et al. [11]. When compared to the DIF values for 30 MPa NSC and 70 MPa HSC, as evaluated by the CEB code [12], UHPC demonstrated lower strain rate sensitivity, particularly at high strain rates.

So far, the development of UHPC materials has been comprehensively reviewed by numerous scholars mainly from the perspective of raw materials [13–15], fibre reinforcement [16–19], additives [20–22], mixture design [23–25], curing regimes [26–28] and so on. While UHPC has already demonstrated exceptional properties [29–36] and emerging applications [37–45], ongoing research efforts continue to optimise UHPC compositions to meet the demand for enhanced material and structural capabilities. Fig. 4 shows the development process of UHPC, starting from the material composition and sample preparation to material properties and potential applications.

Despite considerable efforts in determining cost-effective mix proportions for UHPC, the initial material cost of UHPC still surpasses that of conventional concrete resulting from the high cement content, reactive powder and fibre addition. Nevertheless, the utilisation of UHPC can lead to more sustainable constructions, with potential economic, social and environmental benefits. Utilising UHPC allows for reduced cross-sectional dimensions of structural members, thereby creating additional available space in buildings. UHPC structures also incur lower maintenance costs owing to their improved durability and longer service life. More noteworthily, the exceptional mechanical properties, durability and damage tolerance of UHPC enable the design of robust and durable structures capable of resisting hazardous loads involving blast.

Some earlier review works on the blast performance of UHPC structures are available in the open literature [39,46,47], while the previous overview by Yoo and Banthia [39], which has documented large amount of work in this field, did not incorporate the latest research findings in this rapidly developing field in recent years, particularly in relation to the UHPC-based composite structures. Moreover, the two recent reviews [46,47] lacked a systematic classification in the light of UHPC structural member types. Consequently, the present review study addresses this gap by offering a thorough overview of recent research progress and developments concerning the blast performance of UHPC and UHPC-based composite structures.

1.2. Characteristics of blast loads

According to the explosive confinement, blast load categories acting on the structures could be categorised as confined and unconfined explosions. Unconfined explosions can be further subdivided into free-air burst, air burst and surface burst based on the location of explosives in relation to the ground. In the free-air burst, as depicted in Fig. 5(a), the explosive is positioned near or above the target structures. Blast shock waves propagate spherically from the detonation centre, directly acting on the structures without ground reflection or enhancement. In the air burst, as depicted in Fig. 5(b), the explosive is located at a certain distance suspended over the ground surface and away from the target structures. Part of the initial blast shock waves will interact with the secondary waves reflected from the ground surface, resulting in the amplified shock waves known as the Mach front prior to reaching the

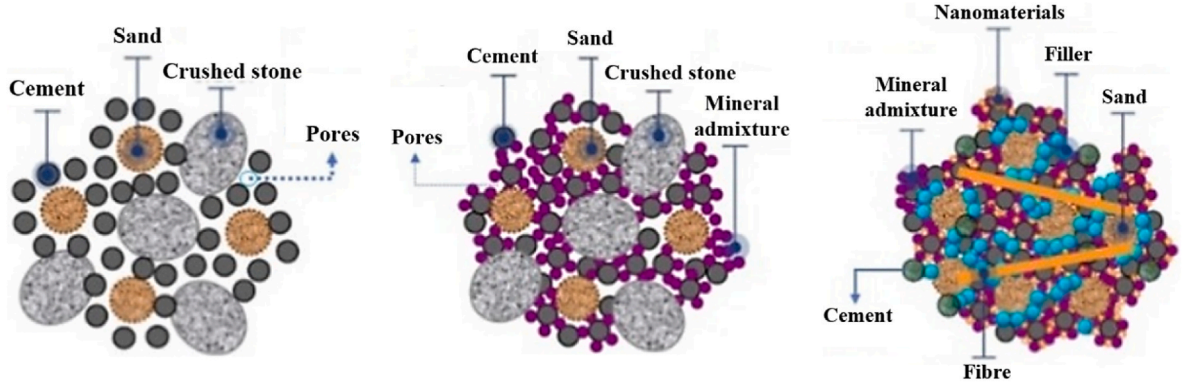

Fig. 1. Material compositions of NSC, HSC and UHPC [2].

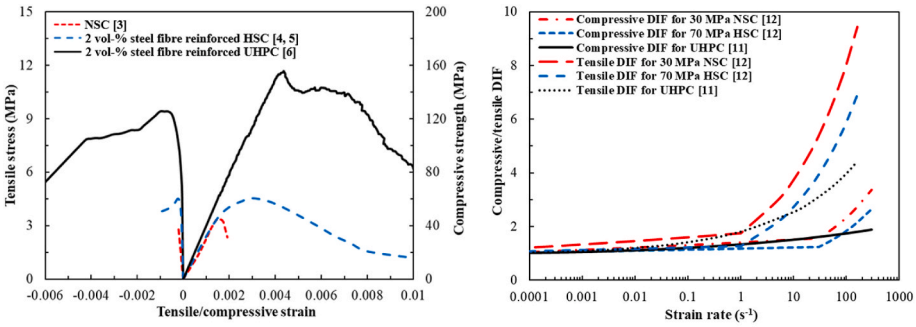

(a) quasi-static uniaxial compressive/tensile behaviours (b) dynamic compressive and tensile behaviours

Fig. 2. Quasi-static and dynamic behaviours of NSC, HSC and UHPC.

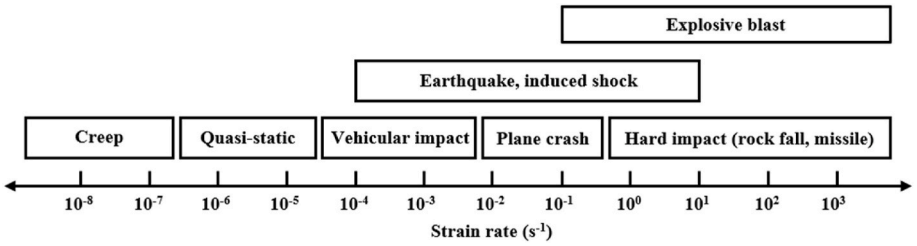

Fig. 3. Typical strain rate intervals applicable to concrete.

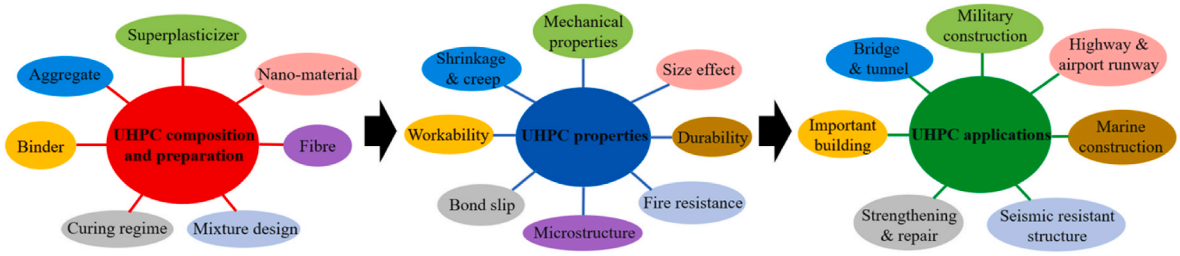

Fig. 4. Development of UHPC: from material composition and sample preparation to material properties and applications.

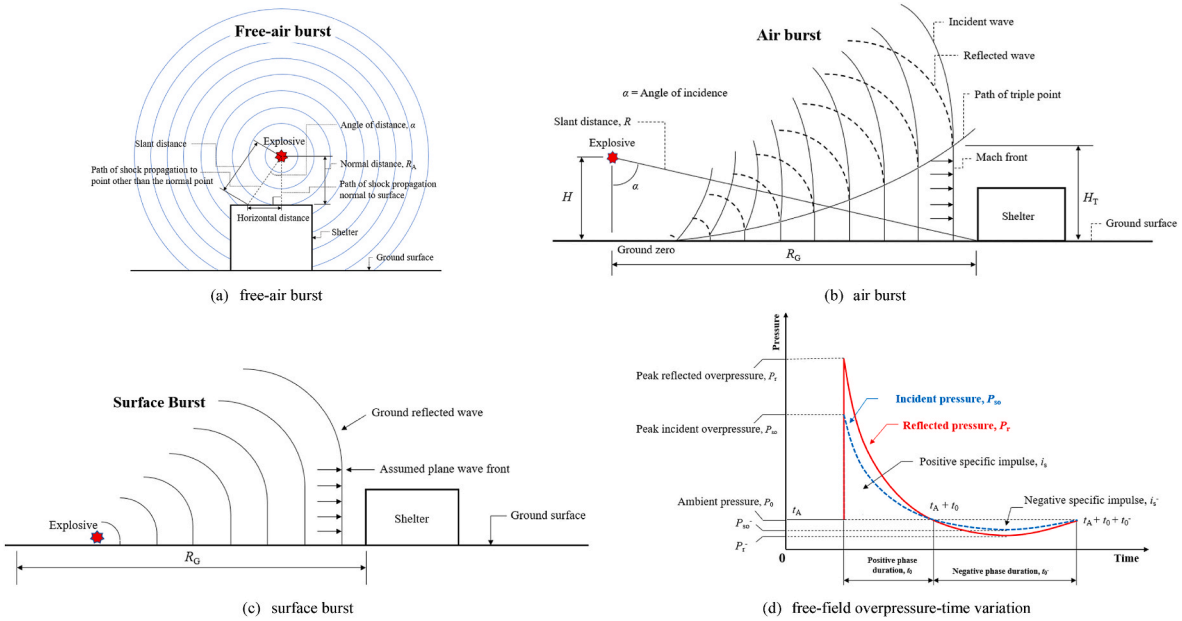

(a) free-air burst (b) air burst

(c) surface burst (d) free-field overpressure-time variation

Fig. 5. Unconfined explosion scenarios and blast overpressure [64].

structures. In the surface burst, as presented in Fig. 5(c), the explosive is situated in close proximity to or directly on the ground surface. This results in the initial blast shock waves being reflected and strengthened at the detonation centre due to ground reflections. Differing from the complex wave patterns of the air burst, the reflected blast shock waves were treated as a single wave, resembling the Mach wave in the air burst while presenting a hemispherical shape. Fig. 5(d) illustrates the typical variation of blast overpressure over time obtained from the free-air burst at a given location on the target structure, wherein the overpressure consists of positive and negative phases. Upon the arrival of the initial shock front at the given location after time t_A, the incident overpressure grows promptly from the ambient pressure P_0 to the peak magnitude P_{so}, followed by an exponential decay returning to P_0 after time t_0. As the blast shock wave continues propagating, the trapped air medium becomes less dense, the overpressure starts to translate into the negative phase until it drops to the peak magnitude P_{so}^-, and then returns to P_0 after time t_0^-. The reflected overpressure follows a similar pattern to the incident overpressure, while it is worth emphasising that when the incident blast wave strikes the structure, the magnitude and impulse of the initial shock wave in both positive and negative phases are reflected and enhanced, resulting in the characteristics of the reflected overpressure. In the design of structures intended to withstand explosions, the negative phase of the overpressure is often omitted from consideration. Nevethless, it has a decisive effect on comparatively flexible structures that are prone to a substantial deformation. In contrast to other two typical destructive events, such as seismic and impact loads as illustrated in Fig. 3, the blast load often produces even shorter duration and greater pressure. The strong motion duration of a typical earthquake record spans several seconds and can extend over a minute, whereas the duration of an unconfined blast pulse induced by a high-explosive detonation is generally on the order of microseconds to milliseconds [48].

To characterise the blast loading effect induced by different masses of trinitrotoluene (TNT) explosives at various standoff distances, the blast scaled distance (Z) can be defined using the explosion similarity law proposed by Hopkinson and Cranz [49]. The blast scaled distance is calculated as $Z = R/W^{1/3}$, where R represents the standoff distance from the detonation centre to the measuring point on the structure surface in the unit of 'm', and W denotes the equivalent mass of TNT explosives in the unit of 'kg'. The blast scaled distance serves as a comparative measure that allows for scaling down the amount of explosive required to generate the same blast shock wave. This is particularly useful in physical tests, because smaller charges can be placed closer to the specimen to simulate larger blasts. Existing guidelines provide definitions for near-field and far-field explosions. The Unified Facilities Criteria (UFC) 3-340-02 [50] defines the near-field explosions as $Z < 0.4$ m/kg$^{1/3}$ and the far-field explosions as $Z \geq 0.4$ m/kg$^{1/3}$. On the other hand, the American Society of Civil Engineers (ASCE) SEI 59-11 [51] considers $Z = 1.2$ m/kg$^{1/3}$ as the critical blast scaled distance to differentiate the near- and far-field explosions. Additionally, updated criteria as reported in Refs. [52–54] define the near-, medium- and far-field explosions, with two notable blast scaled distance thresholds of 0.4 m/kg$^{1/3}$ and 1.0 m/kg$^{1/3}$. It is important to note that the charge weights of various common explosive materials can be converted into an equivalent mass of TNT explosives based on factors such as velocity and heat of detonation [55,56], as well as the maximum blast overpressure and impulse [57].

In addition to the explosive location, charge weight, standoff distance and type, the geometric shape of the explosive also affect the blast overpressure amplitude and impulse distribution. Spherical, cylindrical and rectangular shapes are commonly used for military and commercial explosives, with the spherical shape being deemed the most optimal. This is because the spherical geometry allows for the generation of blast shock waves without directional bias, owing to its axisymmetric nature [58]. Furthermore, it has been recognised that the detonation point within the explosive, geometric dimensions of the cylindrical and square explosives evidently affect the blast load. The influence extent due to the explosive shape is dependent on the blast scaled distance. For far-field explosions particularly when $Z > 5.0$ m/kg$^{1/3}$, the blast load is negligibly affected by the explosive shape, allowing for the assumption of a spherical or hemispherical explosion [59,60]. Neverthless, near-field explosions exhibit an evident dependency on the explosive shape due to the distinct combustion and detonation product [60,61]. Although utilising ideal spherical explosives in real scenarios might be challenging, focusing on explosive geometry can be mitigated if field blast test results align with predictions from guidelines like UFC 3-340-02 [62,63].

1.3. Concrete structural damage under blast loads

The analysis of concrete structures to blast loads is more focused on their critical structural members, since the localised damage may be more evident than the overall response of the entire structure [48]. Extensive studies have been dedicated to exploring the dynamic behaviour of concrete structural members, such as slabs, beams and columns, when subjected to blast loads [57,65–67]. Fig. 6 illustrates a variety of failure modes exhibited by these members, which are influenced by the blast scaled distance Z. At the large blast scaled distance, the structural response tends to be ductile, with flexural failure occurring at the positions where plastic hinges form due to ultimate bending moments. With a reduction in the blast scaled distance, the higher blast overpressure and shorter duration cause a more brittle damage mode, involving combined shear and flexural failure or even direct shear failure. When a blast takes place in close proximity to or directly contacts the concrete structural members, highly localised damage such as crater, scabbing or even perforation might be produced. In the absence of adequate structural redundancy, the loss of individual or several load-bearing concrete components may trigger structural progressive collapse, causing disproportionate damage to the entire building [68,69].

The localised damage observed in concrete structural members as caused by very close-in or contact explosions can be explained through the stress wave propagation theory [38,71]. In this explosive scenario, high compressive stress waves are initially produced, resulting in the crater damage on the front surface of the concrete structural member along with the development of cracks. As the compressive stress waves propagate spherically inside the concrete, they turn into tensile stress waves upon reaching the distal surface to engender the scabbing damage surrounded by cracks. In a more extreme case, if the captured impulse is sufficiently large to conquer the concrete resistance, fractured parts might separate from the distal surface and eject at a certain speed, forming fragments. The stress wave propagation is a cyclic process and will be terminated when the tensile stress waves are consumed and fall

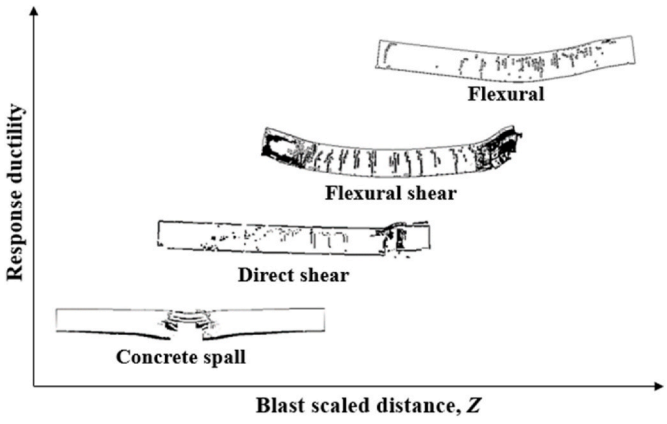

Fig. 6. Typical failure modes of concrete structural members under different blast scaled distances [70].

below the dynamic tensile strength of concrete. Since the stress wave propagation within the concrete occurs much faster than the overall structural response, concrete structural members exposed to the very close-in or contact explosion are less sensitive to boundary conditions as compared to those exposed to medium- and far-field explosions. Two basic classification approaches have been suggested to differentiate the localised damage degree of concrete structural members. The classification I proposed by Morishita et al. [72], as depicted in Fig. 7, identifies three stages of spalling damage, involving crater only, crater and scabbing, and perforation. The classification II proposed McVay [73], as shown in Fig. 8, distinguishes three spalling damage degrees, including mild, moderate and severe, based on the ratio of spalling depth to member thickness.

The determination of the structural safety limit for a particular concrete structural member induced by given blast loading scenarios can be effectively achieved through a pressure-impulse (P-I) diagram [60,74,75]. The P-I diagram, as illustrated in Fig. 9, consists of a range of iso-damage curves, each representing a particular structural damage degree. The P-I diagram includes impulse and pressure asymptotes, which respectively indicate the thresholds of impulse and pressure necessary to attain a specific structural damage degree. It also corresponds to three loading regimes, including impulsive (Regime I), dynamic (Regime II) and quasi-static (Regime III). In Regime I, characterised by an extremely high blast peak pressure and a relatively short blast duration (in comparison to the natural frequency of structural members), the structural damage degree is primarily governed by the blast impulse rather than the blast peak pressure. Regime III, on the other hand, exhibits the opposite pattern to Regime I, wherein the structural damage degree is principally dominated by the blast peak pressure, irrespective of the blast impulse. Regime II represents an intermediate condition, where both the blast peak pressure and impulse jointly contribute to the structural damage degree. The P-I diagram also determines the correlation between blast peak pressure and impulse required for various structural damage degrees. If the combination falls in the upper right of the diagram, it indicates that the structural member will fail, surpassing a certain damage criterion. Conversely, if the combination falls within the lower left region of the diagram, the structural member will not fail at such damage degree. Notably, the damage criterion for the P-I diagram should be selected dependending on the blast loading scenarios and the specific type of structural damage. For instance, when structural members undergo blast-induced flexural damage, parameters such as mid-span deflection [74], maximum support rotation angle [64], peak deflection-span ratio [64] or ductility ratio [76] can be employed as the damage criterion. On the other hand, when structural members suffer shear damage under blast loading conditions, parameters such as shear slip close to the support [77] or average shear strain [78] can be used to define the damage degree.

1.4. Analysis techniques for UHPC structures under blast loads

Physical blast tests offer the most intuitive and effective method to evaluate the dynamic performance of UHPC structures subjected to blast loading conditions. Fig. 10 illustrates a typical setup for field blast (FB) testing of UHPC specimens conducted in a large open space. This testing system provides flexibility in terms of various parameters, including specimen scale and geometry, explosive mass and shape, standoff distance, boundary conditions, instruments for data acquisition and so on. Notably for the blast testing on the column, there are different approaches. The column can be positioned above the ground to simulate blast loading [79]. Alternatively, the column can be buried in an excavated pit, with a portion of the column's lateral surface exposed to the blast shock waves. This configuration helps eliminate the clearing influence, and reduces extra shock wave refraction and reflection [80]. Besides, hydraulic or pneumatic jacks are typically used to provide axial loading in the column during testing. Although the FB test is a commonly employed technique and has been extensively used in recent years, it still presents challenges related to cost, site conditions, facilities, time, safety concerns, etc. [57].

In addition to the FB tests, laboratory testing systems utilising specialised facilities such as blast simulator (BS) and shock tube (ST) have been rapidly developed and increasingly employed in the study of far-field blast resistance for UHPC structures. Fig. 11 illustrates the BS facility at the University of California, San Diego [84], which employs multiple blast generators to simulate distributed impulsive loads on UHPC slabs. However, it shall be noted that the blast generators struggle to accurately reproduce the negative phase of the overpressure owing to the absence of the required tensile force for specimen recoil [57]. Figs. 12 and 13 present the representative ST facilities at the U.S. Army

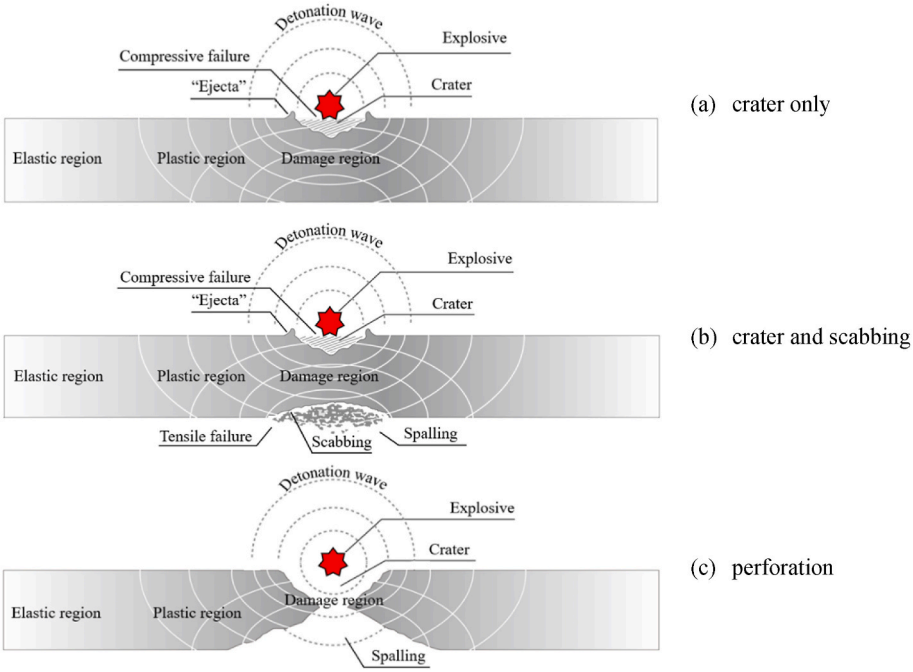

Fig. 7. Localised damage classification I of concrete structural members under contact or very close-in explosions [72].

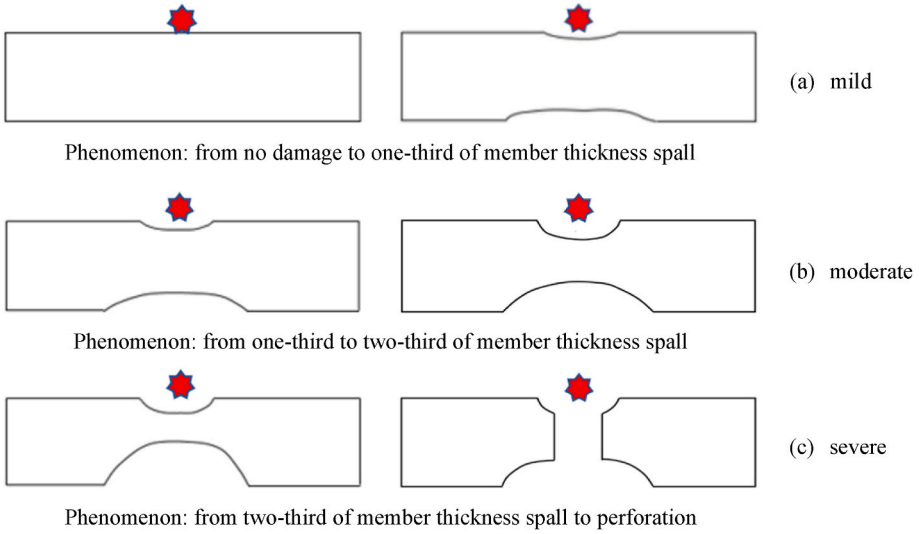

Fig. 8. Localised damage classification II of concrete structural members under contact or very close-in explosions [73].

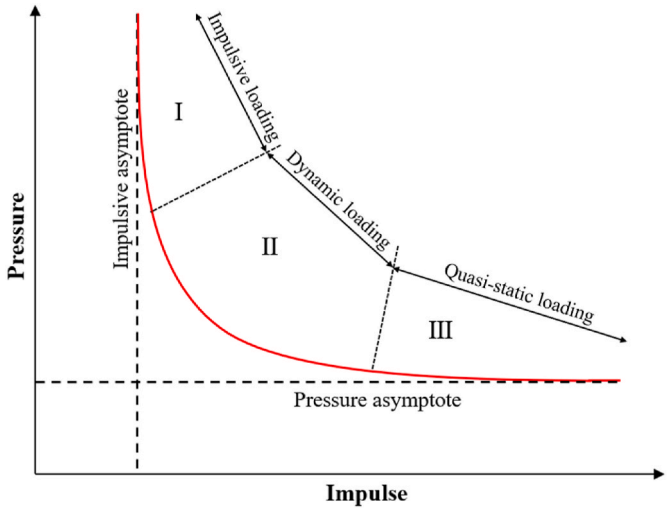

Fig. 9. Schematic diagram of a typical P-I diagram [66].

Corps of Engineers-Engineer Research and Development Centre (USA-CE-ERDC) and the University of Ottawa, utilised for testing UHPC slabs, beams and columns [85–88]. The simulated blast shock waves are produced by a driver through the quick release of compressed gas. These shock waves are then distributed to impulsive loads, uniformly acting on the specimen via load transfer devices. The driver length and pressure can be adjusted to achieve the desired combination of overpressure and impulse. However, conventional ST facilities may struggle with accurate replication of time-dependent gas dynamic scenarios and various flow anomalies [89]. To address these limitations, an advanced ST facility, funded by the Australian National Facility for Physical Blast Simulation (NFPBS), has been developed at the University of Wollongong [90], as depicted in Fig. 14. This facility excels at replicating the entropy gradient and negative phase of the overpressure, offering a reliable far-field explosion environment [90]. It is noteworthy that the blast shock wave profile generated in the ST testing system should be verified through the comparison with actual blast tests, aiming to guarantee that the overpressure-time evolution accurately represents the real blast scenarios [57].

The continuous advancement of powerful computational tools has paved the way for numerical simulations to become a highly efficient approach in the study of UHPC structures under blast loads, thereby either as an alternative or supplement to experimental methods. The most common commercial finite element (FE) programs for explicitly analysing the dynamic response of UHPC structures loaded with blast include ANSYS-DYNA [91], ANSYS-AUTODYN [92], ABAQUS/Explicit [93] and so on [57]. These programs offer a range of material constitutive models that incorporate strength surfaces, damage accumulation, strain rate effect and equations of state (EOS) to simulate the behaviour of concrete [38,94,95]. However, the uniqueness of the UHPC composition, combined with its complex static and dynamic material behaviour, necessitates the calibration or updating of the existing concrete models for precise prediction of the dynamic behaviour of UHPC structures subjected to blast loads.

Blast modelling is another critical factor that determines the efficient and accurate prediction of UHPC structural behaviour under blast loads in the numerical simulations. There are four common methods for blast modelling in the FE programs like ANSYS-DYNA, including the idealised triangular impulse (ITI), CONWEP model, smooth particle hydrodynamics (SPH) and arbitrary Lagrangian-Eulerian (ALE). Each method has its own merits and limitations. The ITI method simplifies the measured overpressure-time curve into an equivalent triangular curve with peak overpressure and positive duration, which is then applied to the loaded surface of UHPC structures for computation. This method is computationally efficient but unable to accurately reproduce the damage caused by non-uniform blast loads in near-field explosions. The semi-empirical CONWEP method utilises keywords like LOAD_BLAST or LOAD_BLAST_ENHANCED to predict overpressure [91]. It allows for defining the equivalent mass of TNT explosives, detonation point and explosion type. Without establishing the air domain and explosive, this method is also efficient in computation, while it lacks the capability to account for the influence of explosive shape on the blast effect. The SPH method builds the explosive using SPH particles without explicitly modelling the air domain. The SPH algorithm is employed to simulate the explosive expansion and interactions between blast shock waves and UHPC structures. This method is only suitable for contact or very close-in explosion scenarios but may have limitations beyond that. The ALE method incorporates Euler elements to model the explosive and air domain, allowing the simulation of blast shock wave propagating in the air medium and its interaction with UHPC structures. Due to the modelling of the air domain, this method is time-consuming, particularly for far-field explosion scenarios. Additionally, the accuracy of numerical outcomes might be influenced by the element size of the air domain. Selecting an appropriate blast modelling method is dependent on the specific blast scenario and desired accuracy level, while considering computational efficiency and limitations associated with each

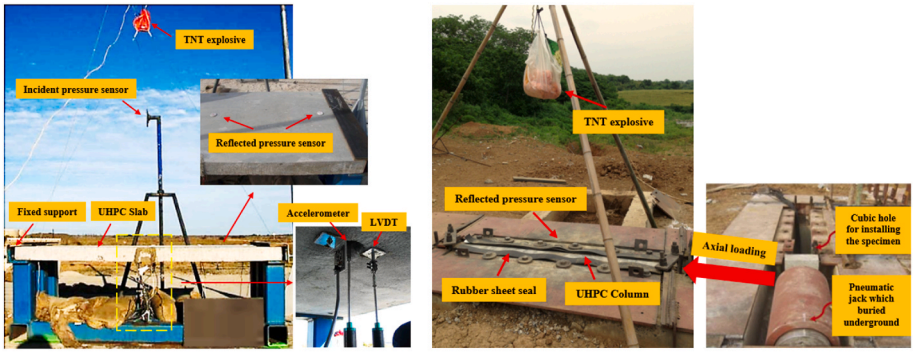

(a) UHPC slab [81] (b) UHPC column [82]

(c) UHPC beam [83]

Fig. 10. FB testing system on UHPC structural members [81].

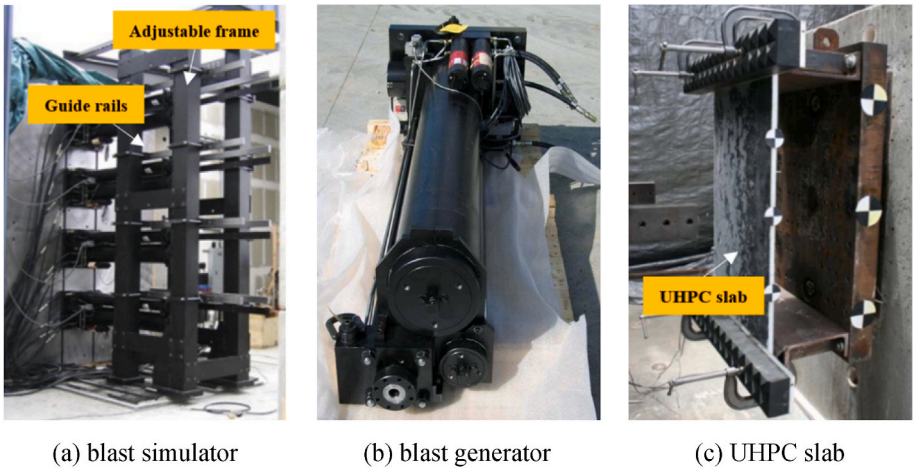

(a) blast simulator (b) blast generator (c) UHPC slab

Fig. 11. BS facility for testing UHPC slabs at the University of California, San Diego [84].

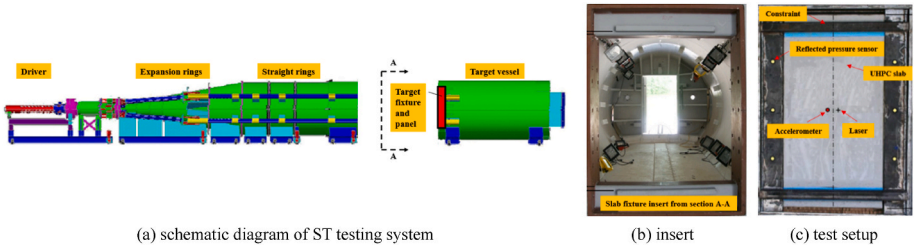

(a) schematic diagram of ST testing system (b) insert (c) test setup

Fig. 12. ST facility for testing UHPC slabs at USACE-ERDC [87].

method.

Several theoretical methods exist for analysing structural responses to blast loadings, including the single degree of freedom (SDOF) [96], finite-difference (FD) [97], modal superposition [98], etc. Among these, the SDOF model gained popularity for its simplicity and consideration of dynamic effects in analysing and designing concrete members against

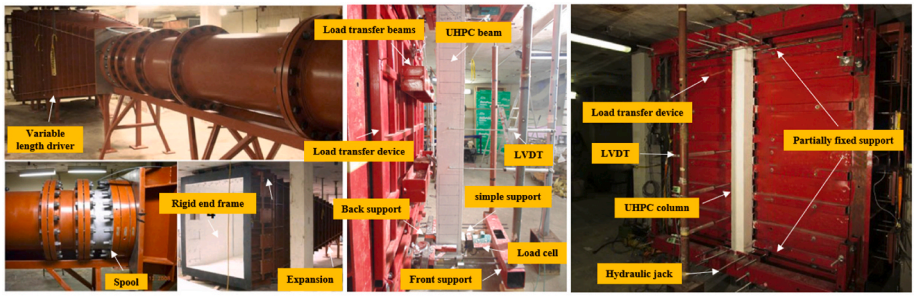

(a) ST testing system [85] (b) test setup on UHPC beam [88] (c) test setup on UHPC column [86]

Fig. 13. ST facility for testing UHPC beams and columns at the University of Ottawa.

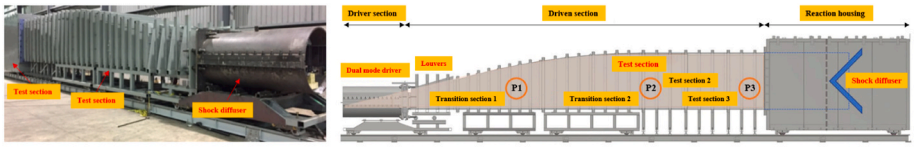

(a) ABLS testing system configurations (b) schematic diagram of ABLS testing system

Fig. 14. Advanced ST facility at the University of Wollongong [90].

blast loads [64,99]. The equivalent SDOF model treats the structural member to an idealised SDOF system with equivalent stiffness, mass and dynamic load (represented by an idealised triangular pulse), depending on the given structural response type. This model is adaptive for far-field explosion scenarios where the blast load is relatively uniform and the structural response type is primarily flexural [100]. However, for scenarios with small blast scaled distances, other response types such as shear or local damage might dominate the structural response. In such cases, the equivalent SDOF model may not be appropriate and needs further modifications so as to accurately predict other response types [100].

2. UHPC structural members under blast loads

Drawing from a wide array of findings from experimental, numerical, and theoretical studies available in the open literature, this section endeavours to provide a comprehensive review and analysis of the dynamic behaviour of UHPC structural members, including slabs, beams and columns, under a variety of blast loading conditions. Simultaneously, comparative analyses regarding the blast performance of UHPC and normal reinforced concrete (NRC) or HSC members are also included under typical blast scenarios to underscore the superiority of UHPC in withstanding blast loads.

2.1. UHPC slabs

Extensive investigations into the blast response and damage behaviour of UHPC slabs, specifically those utilised in building floors and bridge decks, have been conducted. For readers' reference, a summary of these relevant studies, gathered from the open literature sources, can be found in Table 1 in Appendix.

Published research data regarding the blast response of UHPC slabs primarily concentrates on one-way slabs. Ngo et al. [101] conducted surface burst tests using rectangular Hexoline explosives weighing 5000 kg (equivalent to 6000 kg TNT) at a standoff distance of 40 m ($Z = 2.2$ m/kg$^{1/3}$) to compare the far-field blast performance of 2000 mm × 1000 mm × 100 mm pre-stressed and simply-supported Ductal® UHPC and NRC slabs. As presented in Fig. 15, in contrast to the companion NRC slab, the UHPC slab demonstrated remarkable ductility, minimal permanent deflections, and the capacity to absorb substantial energy without fragmentation. As the standoff distance decreased to 30 m ($Z =$ 1.65 m/kg$^{1/3}$), the structural response of the UHPC slab became more pronounced, resulting in the significant deflection, though no major damage was observed likewise. Mao et al. [102] conducted air burst tests using 100 kg TNT explosives at various standoff distances and corresponding numerical simulations, attempting to explore the effect of steel fibre and rebar contents on the far-field explosion response of 3500 mm × 1300 mm × 100 mm simply-supported UHPC slabs. The research outcomes indicated that when $Z > 2.7$ m/kg$^{1/3}$, both the steel fibre and rebar contents had a similar effect in strengthening the blast resistance

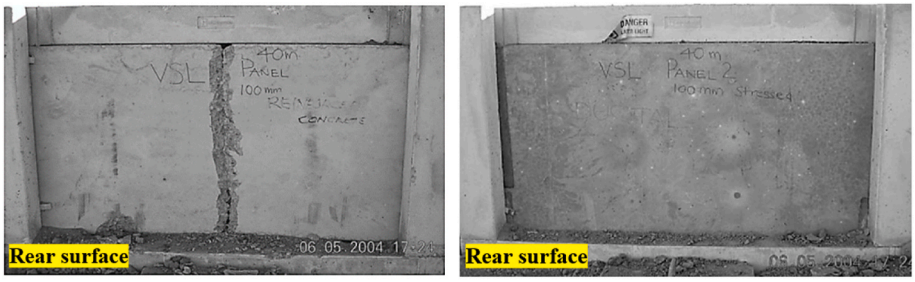

(a) NRC slab (b) Ductal® UHPC slab

Fig. 15. Blast response of 2000 mm × 1000 mm × 100 mm pre-stressed and simply-supported one-way Ductal® UHPC and NRC slabs at $Z = 2.2$ m/kg$^{1/3}$ under surface burst environment [101].

of UHPC slabs, However, when $Z < 2.7$ m/kg$^{1/3}$, the steel rebar content had a more substantial impact on enhancing the UHPC slabs against explosions. In a subsequent study, Mai et al. [103] did a parametric analysis using the validated numerical model to examine the influences of slab thickness and steel reinforcement ratio on the far-field explosion behaviour of UHPC slabs under various magnitudes of Z. Their findings revealed that as the slab thickness decreased, the damage mode transitioned from primarily flexural to a combination of shear and flexural. Additionally, the positive effect as offered by the steel reinforcement ratio on decreasing the maximum mid-span deflection of the slabs more pronounced in the medium-field explosion scenario as compared to the far-field explosion scenario. Wu et al. [104] also confirmed through free-air bust tests that in the case of approximately medium-field explosion (cylindrical Composition B explosives, $Z = 0.37$–0.5 m/kg$^{1/3}$), the UHPC slab with steel reinforcement exhibited a superior performance in comparison to the unreinforced UHPC slab. Building upon these findings, Li et al. [62] further designed reinforced UHPC slabs measuring 2000 mm × 1000 mm × 100 mm with partially fixed boundary conditions, and then tested their behaviour in the free-air burst scenario utilising spherical Composition B explosives (1–14 kg TNT equivalent). As shown in Fig. 16, the UHPC slab displayed a flexural response within the elastic range at $Z = 3.05$ m/kg$^{1/3}$. As Z decreased from 0.5 m/kg$^{1/3}$ to 0.41 m/kg$^{1/3}$, the UHPC slab shifted from the plastic range to complete failure. Also noted, the yielding strength of the steel reinforcement played a prominent role in reducing the mid-span deflections of UHPC slabs when subjected to medium-field explosions. Subsequently, Lin [105] implemented a parametric study using a validated numerical model to explore the effects of steel reinforcement ratio on the mediuem- and far-field blast performance of UHPC slabs under free-air burst conditions. The numerical outcomes indicated that the effect of the steel reinforcement ratio could be disregarded when the UHPC slab underwent far-field explosions ($Z = 1.3$ m/kg$^{1/3}$). Increasing the steel reinforcement ratio proved effectiveness in enhancing the resistance of UHPC slabs to medium-field explosions ($Z = 0.5$ m/kg$^{1/3}$), but the improvement became less pronounced when the ratio exceeded a certain threshold, i.e. 1.4 vol-%. Su et al. [54] adopted 4 kg cylindrical TNT explosives at standoff distances spanning from 0.79 m to 1.27 m ($Z = 0.5$–0.8 m/kg$^{1/3}$) to generate a free-air burst environment for testing the blast behaviour of reinforced and simply-supported UHPC slabs with dimensions of 2400 mm × 1000 mm × 100 mm. Under the medium-field explosion, flexural response was observed on the slab, and the flexural damage of UHPC slabs became more severe as Z decreased, yielding larger mid-span deflection coupled with an increased number of cracks. Ellis et al. [87] utilised the BS facility to test unreinforced and simply-supported UHPC slabs having dimensions of 1626 mm × 864 mm × 50 mm under reflected impulse loads varying from 0.77 MPa ms to 2.05 MPa ms. The study revealed that the unreinforced UHPC slabs experienced failure at reflected impulse levels ranging from 0.97 MPa-sec to 1.47 MPa-sec. Utilising a hierarchical multi-scale model, the numerical findings demonstrated that factors such as steel fibre geometry and content that increased the energy dissipation were crucial in enhancing the blast resistance of unreinforced UHPC slabs. Through near-field explosion tests (25 kg rectangular TNT explosives at a standoff distance of 0.45 m, $Z = 0.15$ m/kg$^{1/3}$) upon two full-scale reinforced bridge decks under free-air burst conditions [106], the positive influence of steel fibre content and strength on improving the blast performance was also demonstrated. As observed, the UHPC bridge deck with higher steel fibre content and strength effectively inhibited the concrete spallation, though it did not show significant advantages in reducing the mid-span permanent deflection.

The investigation into the anti-explosion performance of two-way UHPC slabs is less conducetd. Yi et al. [107] carried out medium-field explosion tests on an unreinforced UHPC slab measuring 1000 mm × 1000 mm × 150 mm under the free-air burst circumstance. The UHPC slab, clamped on all four sides, underwent the 15.88 kg spherical ANFO explosion (13.02 kg TNT equivalent) at a standoff distance of 1.5 m ($Z = 0.64$ m/kg$^{1/3}$). Comparing to the companion reinforced slabs made of NSC and HSC, the UHPC slab exhibited decreased maximum and residual deflections, more controlled cracking with less spalling damage and higher energy absorption capacity. These benefits were ascribed to the positive influence of short steel fibres in the UHPC slab. Under a similar burst circumstance, Mao et al. [108] experimentally and numerically assessed the medium-field explosion response of 660 mm × 660 mm × 25 mm unreinforced and fully fixed UHPC slabs with various steel fibre reinforcements to 0.2–1.1 kg spherical PE4 explosives (0.24–1.32 kg TNT equivalent) at a fixed standoff distance of 0.5 m ($Z = 0.46$–0.8 m/kg$^{1/3}$). The study determined that the fibre length slightly affected the blast resistance of UHPC slabs, but there was a noticeable improvement in the blast resistance when the fibre content was increased from 2 vol-% to 6 vol-%, as depicted in Fig. 17.

Dragos et al. [109] incorporated an advanced moment-rotation analysis technique into the FD model to analyse the dynamic response of one-way reinforced UHPC slabs subjected to blast loads. Adopting the verified FD model and considering the ultimate rotation of the plastic hinge as the failure criterion, a normalised P-I diagram accompanied by two normalisation equations was established for UHPC slabs. Fig. 18 illustrates this diagram, in which the coordinates, P_r and I, need to be respectively scaled up by P_{rmin} and I_{min}, as given by the following normalisation equations:

$$P_{rmin} = 1.8\left(k_{yp}k_{duc}D^{0.584}L^{-2}M_u\right) \tag{1a}$$

$$I_{min} = 57.04\sqrt{W_e D^{1.231}L^{-0.5}/k_{yi}} \tag{1b}$$

where P_{rmin} represents the minimum peak reflected overpressure; $k_{yp} = \left(\frac{M_y}{M_u}\right)^{0.293}$ denotes the yield factor/pressure; M_y and M_u respectively denote the yield and ultimate moments; $k_{duc} = \left(\frac{\theta_u}{M_u}\right)^{0.168}$ denotes the dynamic ductility shape factor; θ_u denotes the ultimate rotation; Ds and

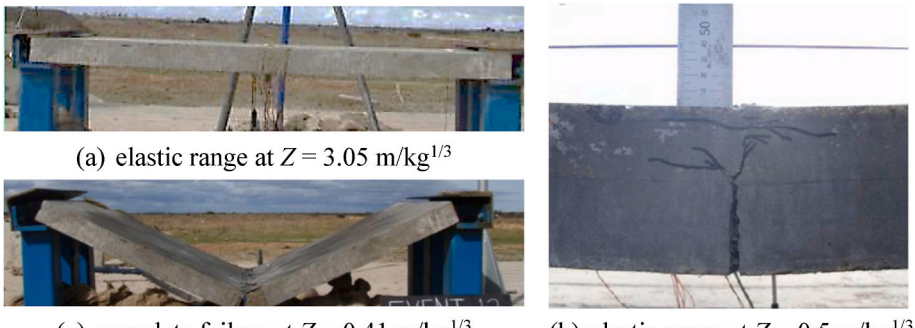

(a) elastic range at $Z = 3.05$ m/kg$^{1/3}$

(c) complete failure at $Z = 0.41$ m/kg$^{1/3}$

(b) plastic range at $Z = 0.5$ m/kg$^{1/3}$

Fig. 16. Damage mode of 2000 mm × 1000 mm × 100 mm reinforced and partially fixed one-way Ductal® UHPC slabs under free-air burst environment [62].

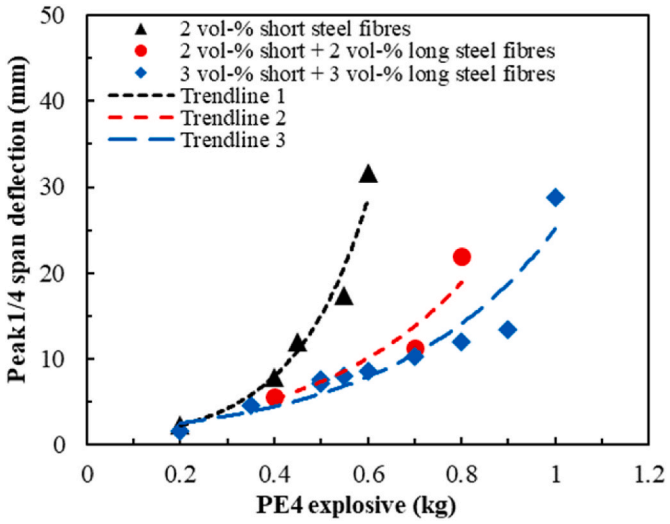

Fig. 17. Peak 1/4 span deflection versus PE4 explosive weight for 660 mm × 660 mm × 25 mm unreinforced and fully fixed two-way UHPC slabs with various steel fibre contents under free-air burst environment [108].

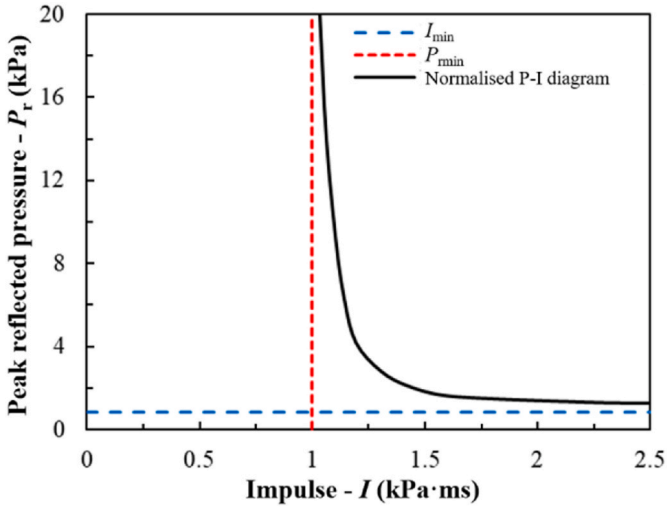

Fig. 18. Normalised P-I diagram for UHPC slabs under blast loads [109].

L_s represent the slab depth and span length, respectively; I_{min} represents the minimum impulse; $W_e = M_u\theta_u$ denotes the energy absorption capacity factor; $k_{yi} = \frac{M_y}{M_u}$ denotes the yield factor/impulse. The normalised P-I diagram is applicable for the generic assessment of UHPC slabs with a variety of sectional and material properties in resisting blast loads.

In a more recent investigation conducted by Hou et al. [78], an improved P-I diagram was put forward to quantitatively evaluate the multiple failure modes of reinforced one-way UHPC slabs subjected to blast loads. The establishment of the P-I diagram relied on two loosely-coupled SDOF models for flexural and shear responses, utilising the support rotation θ and average shear strain γ as the respective failure criteria. Fig. 19(a) presents the P-I diagram incorporating multiple failure modes for a standard one-way UHPC slab. The dimensions of the slab were 4000 mm × 1000 mm × 200 mm, and it was clamped at the short edges. The slab had the uniaxial compressive strength of 100 MPa. The longitudinal reinforcement ratio was 2.8 vol-%, and the load level (i.e. the ratio of the imposed load to the slab bending capacity) was 0.3. The P-I diagram was separated into five regions, including region I (no failure), region II/V (shear failure), region III (flexural failure) and region IV (flexural-shear failure). Notably, in region V, the shear fracture occurred along with shear and flexural damages. Nevertheless, as the flexural damage at the slab mid-span did not have enough time to develop when the shear fracture appeared at the supports, this region was still considered as the shear failure region. Thereafter, parametric studies were performed in their investigation to assess the influences resulting from various factors on the failure modes depicted in the P-I diagrams for UHPC slabs, as illustrated in Fig. 19(b)–(g). As expected, the asymptotes of the P-I diagrams displayed an upward trend with increasing the slab thickness, longitudinal reinforcement ratio and uniaxial compressive strength of UHPC. Conversely, these values exhibited a downward trend with an increase in the slab span. Regarding the load level, a slight increase in the value led to a reduction in the asymptote of the flexural failure P-I curve, while its effect on the asymptotes of the shear failure P-I curves was disregarded. Shifting from the clamped to simply-supported boundary condition caused a noticeable decrease in the asymptotic value of the flexural failure P-I curve, whereas the asymptotic values of the shear failure P-I curves remained nealy unchanged. Drawing from the findings of the parametric studies, an empirical equation was derived to describe the P-I diagrams of multiple failure modes for reinforced one-way UHPC slabs subjected to blast loads, which is given by:

$$(P - P_a)(I - I_a) = \left(\frac{P_a}{2} + \frac{I_a}{2}\right)^m \tag{2}$$

where P_a and I_a respectively denote the pressure and impulse asymptotes, which can be expressed as follows:

1) For flexural failure:

$$P_{fa} = \left(n_{L1} n_{H1} n_{\rho 1} n_{f_c 1} n_{\eta 1} n_{s1}\right) P_{tfa} \tag{3a}$$

$$I_{fa} = \left(n_{L2} n_{H2} n_{\rho 2} n_{f_c 2} n_{\eta 2} n_{s2}\right) I_{tfa} \tag{3b}$$

2) For shear failure:

$$P_{sa} = \left(n_{L3} n_{H3} n_{\rho 3} n_{f_c 3} n_{\eta 3} n_{s3}\right) P_{tsa} \tag{4a}$$

$$I_{sa} = \left(n_{LA} n_{H4} n_{\rho 4} n_{f_c 4} n_{\eta 4} n_{s4}\right) I_{tsa} \tag{4b}$$

where P_{tfa}, I_{tfa}, P_{tsa} and I_{tsa} represent the asymptotes for the standard UHPC slab. The variable n with different subscripts represents the influence of various factors on the asymptotes, including slab span (L_s), slab thickness (H_s), longitudinal reinforcement ratio (ρ), uniaxial compressive strength of UHPC (f_c), load level (η) and boundary condition (s). The shape coefficient m denotes the shape coefficient, which could be constantly taken as 1.82 for the shear failure P-I curves. For the flexural failure P-I curve, m was determined by:

$$m = s\left(-1.29 L_s^{0.1} + 2.48\right)\left(3.3 H_s^{0.04} - 2.1\right) \tag{5}$$

where s was taken as 1.62 and 1.5 for clamped and simply-supported UHPC slabs, respectively.

In contrast to the evident structural response observed in medium- and far-field explosion scenarios, the prevailing damage mode in UHPC slabs in very close-in or contact explosion scenarios is highly localised, and the blast response is not sensitive to the boundary conditions. Li et al. [110] experimentally assessed the resistance of a 100 mm thick UHPC slab reinforced with 2 vol-% steel fibres (without steel rebars) to contact explosions (1 kg cylindrical TNT explosive), and compared its performance with an NRC slab under the identical blast conditions, as depicted in Fig. 20. It was observed that though the UHPC slab exhibited a damage mode akin to that of the NRC slab, the dimensions of the localised damage, especially on the distal surface, were significantly reduced. This phenomenon could be elucidated through two primary factors. Initially, the excellent dynamic strength and toughness of UHPC,

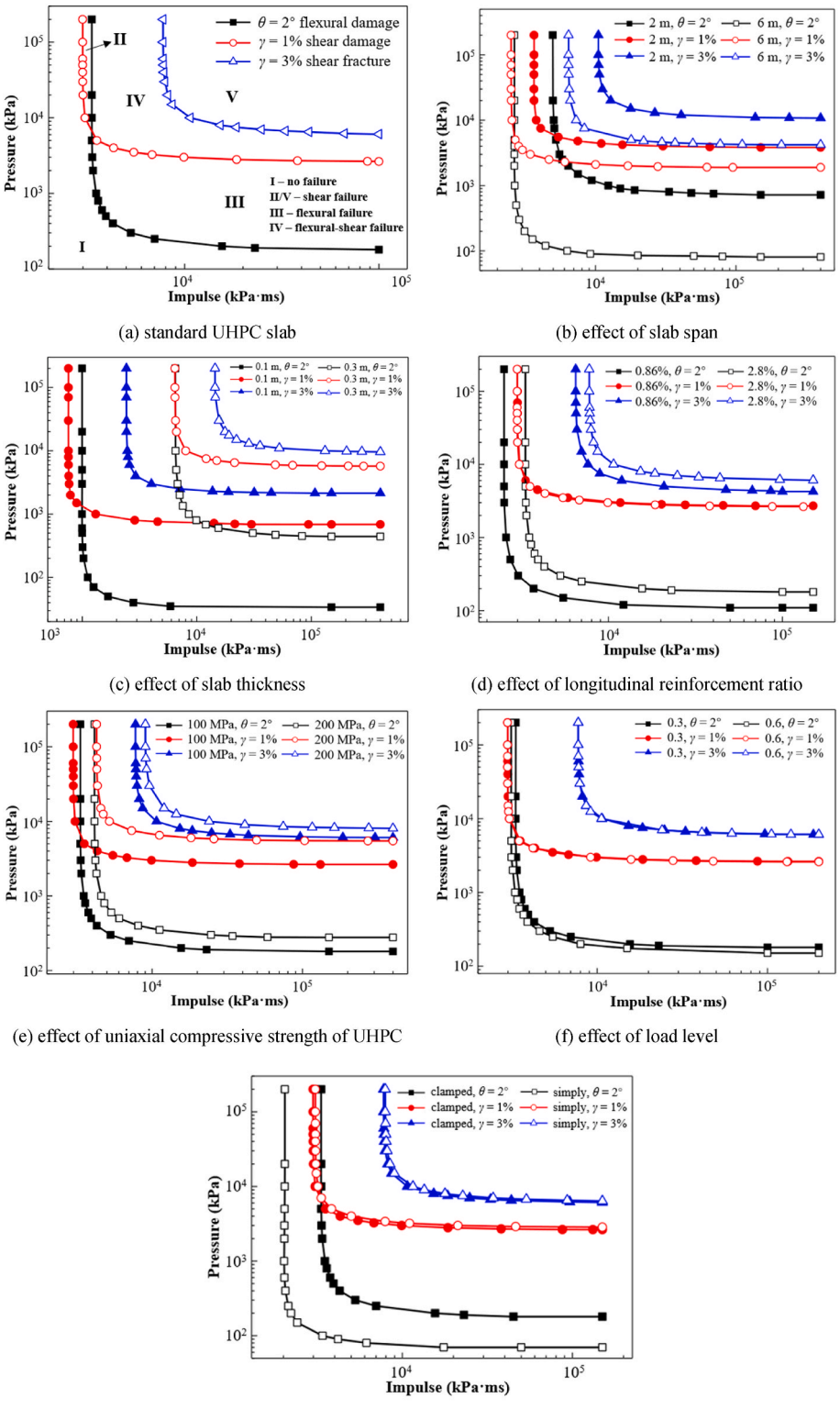

Fig. 19. P-I diagrams of multiple failure modes and influencing factors for one-way UHPC slabs under blast loads [78].

along with the frictional pull-out behaviour of steel fibres, helped dissipate blast stress waves propagating within the slab. Secondly, the incorporation of steel fibres within the UHPC slab afford a notable bridging effect that hinders the separation of cracked-off parts and the further development of cracks. Although research on the influence of volumetric content of steel fibres on the contact detonation resistance of UHPC slabs is still limited, Luccioni et al. [111] experimentally observed that augmenting the content of hooked-end steel fibres from 0.5 vol-% to 1 vol-% only had a limited improvement in the contact explosion resistance of ultra-high strength concrete (UHSC) slabs. While more steel fibres indeed strengthen the material properties of UHPC, the threshold for volumetric content that enhances the blast energy absorption capacity of UHPC slabs remained ambiguous and potentially dependent on UHPC compositions or fibre geometry [38]. To quantitatively assess the

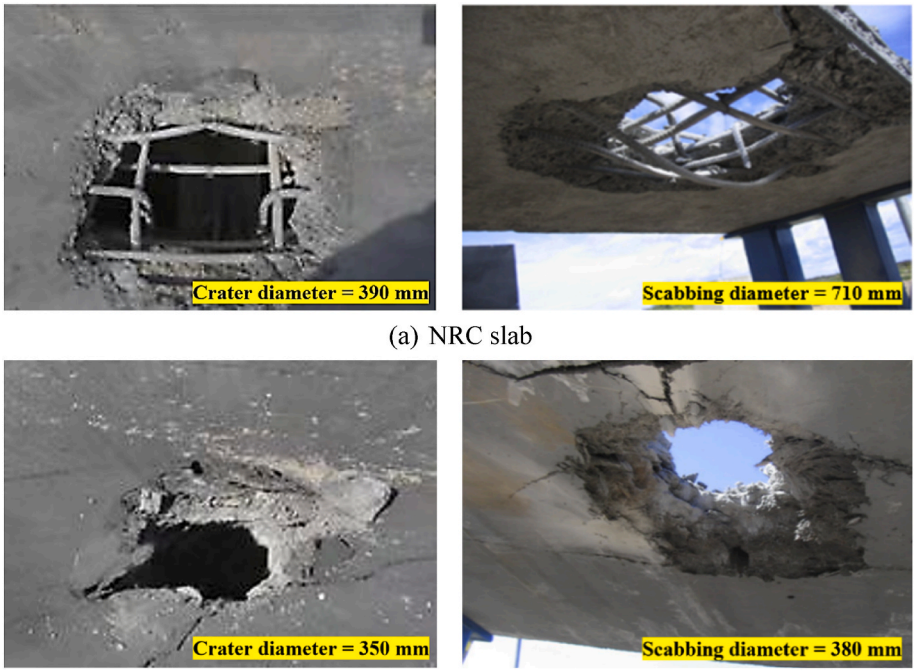

Fig. 20. Localised damage of 100 mm thick NRC and UHPC slabs under 1 kg TNT contact explosion [110].

effect of slab thicknesses and longitudinal reinforcement number on promoting the blast performance of UHPC slabs, Li et al. [71] executed a sequence of contact explosion tests using 0.1 kg or 1 kg cylindrical TNT explosives. It was found that approximately doubling the longitudinal reinforcement number yielded only a minor effect on reducing the localised damage area, indicating that the confinement effect offered by the steel reinforcement was less prominent. As expected, increasing the slab thickness proved effective in mitigating the localised damage and side concrete cracking of UHPC slabs induced by contact explosions. The positive role as played by the slab thickness in resisting contact explosions was also confirmed in experimental investigations by Wan et al. [112].

Predictions of the UHPC spallation caused by contact explosions can be made through available empirical models. Based on classification I (as shown in Fig. 7), Morishita et al. [72] developed a set of empirical equations with respect to the slab thickness (H_s) and TNT equivalent (W) to assess the localised damage degree of NRC slabs under contact explosions. Building upon this research, Liu et al. [113] calibrated the empirical equations to be applicable for UHPC slabs based on numerical simulations, yielding the following equations:

For 'crater only', $H_s / W^{1/3} > 0.22$ (6a)

For 'crater and scabbing', $0.135 < H_s/W^{1/3} \leq 0.22$ (6b)

For 'perforation', $H_s / W^{1/3} \leq 0.135$ (6c)

In a later numerical study, based on classification II (as presented in Fig. 8), Liu et al. [38] proposed additional empirical models to predict the localised damage degree of UHPC slabs with the geopolymer binder under contact explosions, as given by:

For 'mild' damage, $H_s / W^{1/3} > 0.21$ (7a)

For 'moderate' damage, $0.15 < H_s/W^{1/3} \leq 0.21$ (7b)

For 'severe' damage, $H_s / W^{1/3} \leq 0.15$ (7c)

The proposed empirical models were compared with the existing test data on UHPC slabs under contact explosions [71,111,112,114], as depicted in Fig. 21. The analysis revealed that the aforementioned empirical models exhibited a reasonable capability in evaluating the localised damage degree of UHPC slabs exposed to contact explosions, according to both classification criteria.

Besides the localised damage, secondary fragmentation of UHPC structural members caused by very close-in or contact explosion is another particular concern that poses risks to human safety and structural integrity. Li et al. [71] carried out experimental evaluations on the blast-induced fragment distributions of three UHPC slabs with varying thicknesses (120 mm and 150 mm) and numbers of longitudinal rebar on each side (5 and 9) against 1 kg TNT contact explosions. Fig. 22(a) and **(b)** indicate that the fragments originating from the UHPC slab exhibit greater irregularity compared to those originating from the NRC slab. This irregularity can be attributed primarily to the inclusion of fiber reinforcement. As shown in Fig. 22(c), the UHPC slab produced significantly fewer fragments in comparison to the NRC slab when subjected to the identical blast loading conditions, and the weights of fragments passing through each sieve level were lower for the UHPC slab. As depicted in Fig. 23, increasing the slab thickness and the number of longitudinal rebars helped suppress fragment generation from UHPC slabs exposed to contact explosions. Through the sieve analysis and data fitting, it was determined that the Log-normal distribution model was well-suited for representing the sizes of fragments generated from UHPC slabs, and the model is given by:

$$P(\langle D_f) = \frac{1}{2}\left[1 + \mathrm{erf}\left(\frac{\ln x - \mu}{\sigma\sqrt{2}}\right)\right] = \frac{1}{2}\mathrm{erfc}\left(-\frac{\ln x - \mu}{\sigma\sqrt{2}}\right) = \varphi\left(\frac{\ln x - \mu}{\sigma}\right) \quad (8)$$

where $P(<D_f)$ represents the cumulative weight percentage of fragments with a diameter smaller than D_f; erf and erfc denote the error and complementary error functions, respectively; μ and σ respectively represent the location and scale coefficients; φ denotes the cumulative distribution function (CDF) based on the standard normal distribution. As illustrated in Fig. 23, the size distribution of fragments generated from UHPC slabs exhibited fair agreement with the Log-normal distribution model after fitting the coefficients μ and σ.

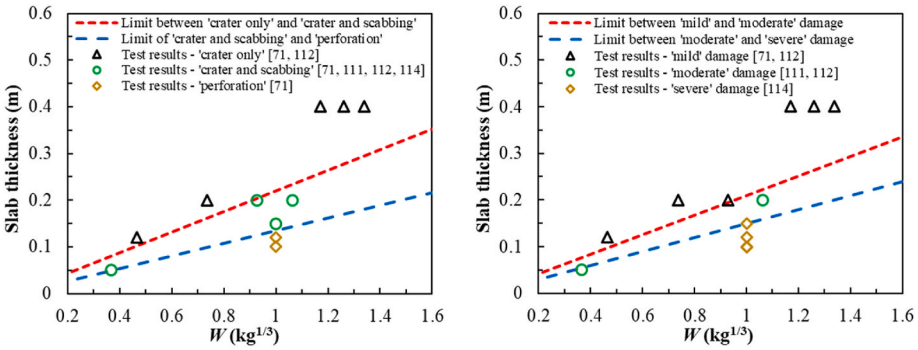

Fig. 21. Empirical models to evaluate the local damage of UHPC slabs under contact explosions.

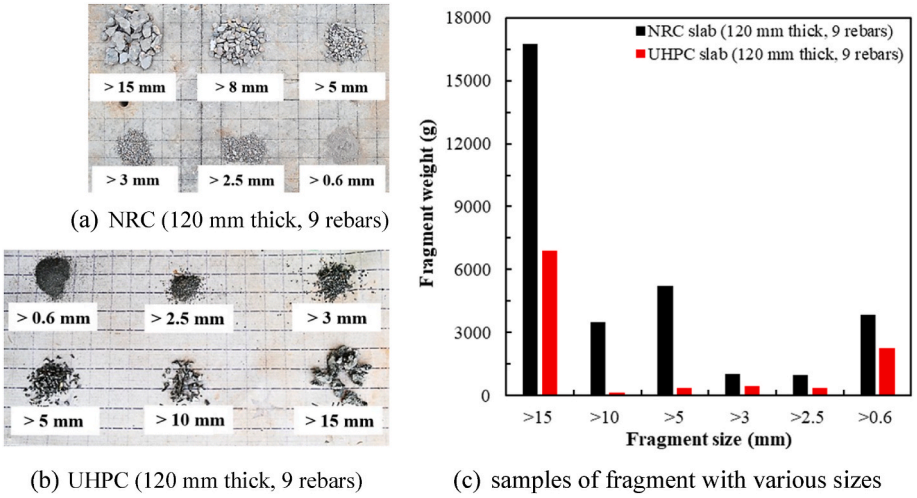

Fig. 22. Fragment samples of 120 mm thick NRC and UHPC slabs after 1 kg TNT contact explosions [71].

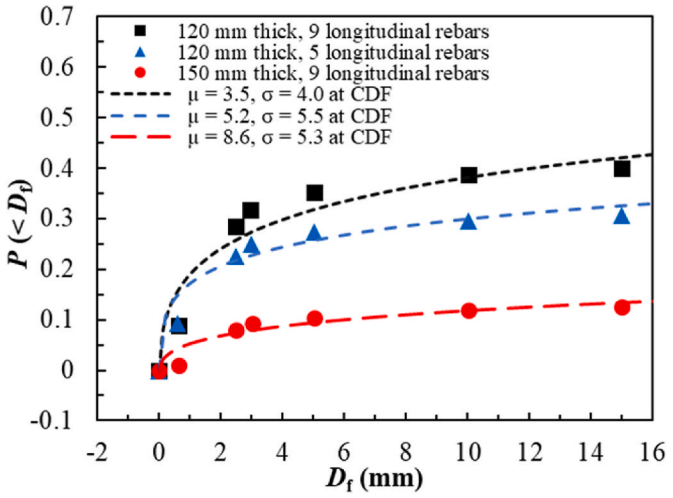

Fig. 23. Log-normal distribution of fragment sizes generated from UHPC slabs [71].

2.2. UHPC beams

Until now, the available literature has only encompassed a restricted array of investigations focused on UHPC beams exposed to free-air burst scenarios. An overview of these studies can be found in Table 2 in Appendix.

Yan et al. [83] executed near-field blast tests at a fixed standoff distance of 0.25 m with various charge weights of cylindrical TNT explosives (1–2 kg, Z = 0.2–0.25 m/kg$^{1/3}$) as well as the supplymentary numerical simulations to assess the blast-resistant capabilities of 2440 mm × 125 mm × 250 mm simply-supported UHPC beams reinforced with glass fibre reinforced polymer (GFRP) rebars. The investigation aimed at the influences resulting from concrete type, transverse reinforcement (stirrup), reinforcement type and ratio on the resistance of UHPC beams to withstand blast loads. Fig. 24 depicts the results under the same blast loading scenario at Z = 0.22 m/kg$^{1/3}$, where the NRC beam experienced shattering at mid-span with extensive concrete fragmentation and GFRP rebar rupture. In contrast, the UHPC beam only suffered localised damage on the front face, with several cracks discernible within the flexural zone. GFRP rebars demonstrated significant advantages over normal-strength steel (NSS) and high-strength steel (HSS) rebars in enhancing the blast resistance of UHPC beams, contributing to substantial rebound deflection and minimised residual deflection, as presented in Fig. 25(a). By incorporating compressive longitudinal reinforcement, rebound failure in GFRP reinforced UHPC beams due to moment reversal under blast loads was effectively prevented, which is depicted in Fig. 25(b). Moreover, as shown in Fig. 25 (c), the synergy between compressive and tensile longitudinal reinforcements, coupled with the incorporation of transverse reinforcement, significantly contributed to the reduced deflection and limited occurrence of localised damage. It was also found that 16 mm diameter GFRP longitudinal reinforcement provided the most effective

(a) NRC beam (b) UHPC beam

Fig. 24. Comparison of the response of 2440 mm × 250 mm × 125 mm simply-supported NRC and UHPC beams with GFRP rebars to free-air burst at $Z = 0.22$ m/kg$^{1/3}$ [83].

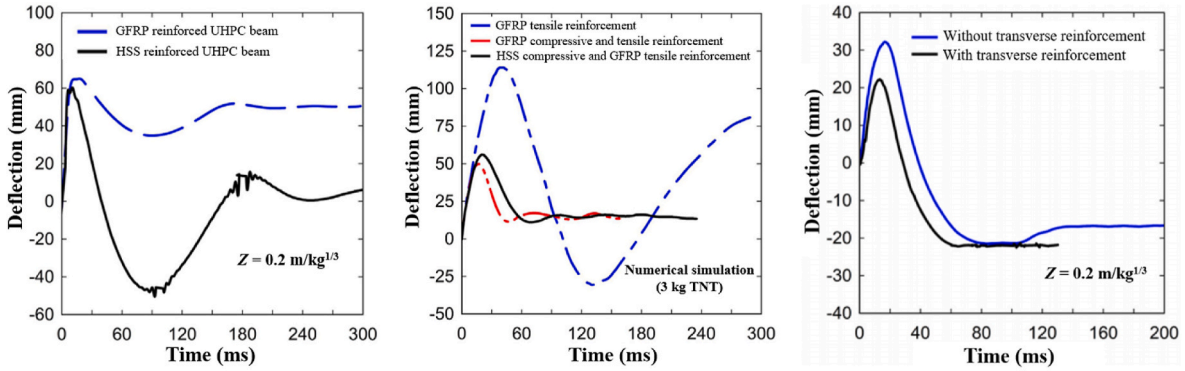

(a) effect of reinforcement type (b) effect of compressive reinforcement (c) effect of transverse reinforcement

Fig. 25. Effects of reinforcement type, compressive and transverse reinforcements on the mid-span deflection of UHPC beams under blast loads [83].

enhancement in the blast performance of UHPC beams, outperforming 12 mm and 20 mm diameter reinforcements.

Guertin-Normoyle [88] systematically investigated the single and repeated far-field explosion performance of simply-supported UHPC beams, measuring 2440 mm × 125 mm × 250 mm, implemented by the ST facility at reflected impulse levels approximately between 0.25 MPa ms and 1.09 MPa ms. This study explored the influences of various design parameters, including steel rebar type, longitudinal reinforcement ratio, transverse reinforcement, steel fibre type and content on the blast performance of UHPC beams. The test results highlighted the significant benefits of using high strength reinforcement in resisting blast loads, as it notably enabled the full capacity of UHPC to be utilised effectively. In addition, increasing the reinforcement ratio had a substantial positive effect on blast performance and prevented bar rupture. Among the steel fibres, those with larger aspect ratios demonstrated a more pronounced influence on the blast resistance. While the steel fibre content between 1 vol-% and 3 vol-% had a limited impact on blast resistance, further studies were recommended to evaluate its effects more comprehensively. The inclusion of transverse reinforcements evidently improved shear resisting strength and prevented brittle shear failure in the UHPC beams. In a later research, Almustafa and Nehdi [115] employed a machine-learning method to forecast the maximum mid-span deflection of UHPC beams against far-field explosions. This was followed by a parametric investigation aimed at assessing the effects arising from variations in fiber properties. In the case of UHPC beams with NSS rebars, augmenting the steel fiber content had a limited impact at lower blast magnitudes and even reduced blast resistance at higher blast magnitudes. However, in UHPC beams with HSS rebars, increasing the steel fibre content improved blast resistance until reaching a critical threshold, beyond which blast resistance decreased. It was also noted that the use of shorter steel fibres with a larger aspect ratio effectively enhanced the blast capacity of UHPC beams.

2.3. UHPC columns

In recent years, there has been a notable rise in the number of studies dedicated to investigating the blast resistance of UHPC columns, since they are critical load-bearing components in structural systems. To offer a comprehensive overview, a collection of published studies delving into the blast performance of UHPC columns has been outlined in Table 3 in Appendix.

Xu et al. [82] experimentally assessed the blast resistance of reinforced and fully fixed UHPC columns with dimensions of 2500 mm × 200 mm × 200 mm. In their study, cylindrical emulsion explosives with charge weights varying from 1.4 kg to 48 kg (equivalent to 1–35 kg TNT) were used at a consistent standoff distance of 1.5 m (Z = 0.5–1.5 m/kg$^{1/3}$). In Fig. 26, the results showed that at $Z = 0.6$ m/kg$^{1/3}$, the HSC column suffered notable concrete spalling damage on both the top and bottom surfaces, while the UHPC column displayed superior explosion resistance, with only minor flexural cracks observed at the bottom surface and limited permanent mid-height deflections. Also observed in Fig. 26, the mid-span deflection of axially loaded specimens was lower than those without axial load, since the presence of the axial load changed the boundary condition of the columns and restricted the end rotation. The impact of the change in boundary conditions dominated over the P-delta effect, leading to a diminished mid-height deflection. The same batch of blast tests on UHPC columns (17.5–35 kg TNT equivalent at a standoff distance of 1.5 m, Z = 0.46–0.58 m/kg$^{1/3}$) as conducted by Li et al. [116] indicated that the steel fibre shape (i.e. straight and twisted) had a minimal impact on the anti-explosion performance.

Burrell [117] conducted an experimental investigation on partially fixed UHPC columns with dimensions of 2468 mm × 152 mm × 152 mm to assess their performance under combined simulated blast loads and axial loads using the ST facility. The single and repeated reflected impulse in this experiment ranged approximately from 0.013 MPa ms to 0.1 MPa ms, and the axial load applied was 294 kN (axial load ratio of 0.3). The test outcomes revealed that the residual deflections of the UHPC columns exhibited a pseudo-linear decrease with an escalation in the fibre content up to 4 vol-%, while a subsequent elevation in the fibre content from 4 vol-% to 6 vol-% led to an augmentation in the residual deflections. Additionally, it was observed that a narrower spacing of

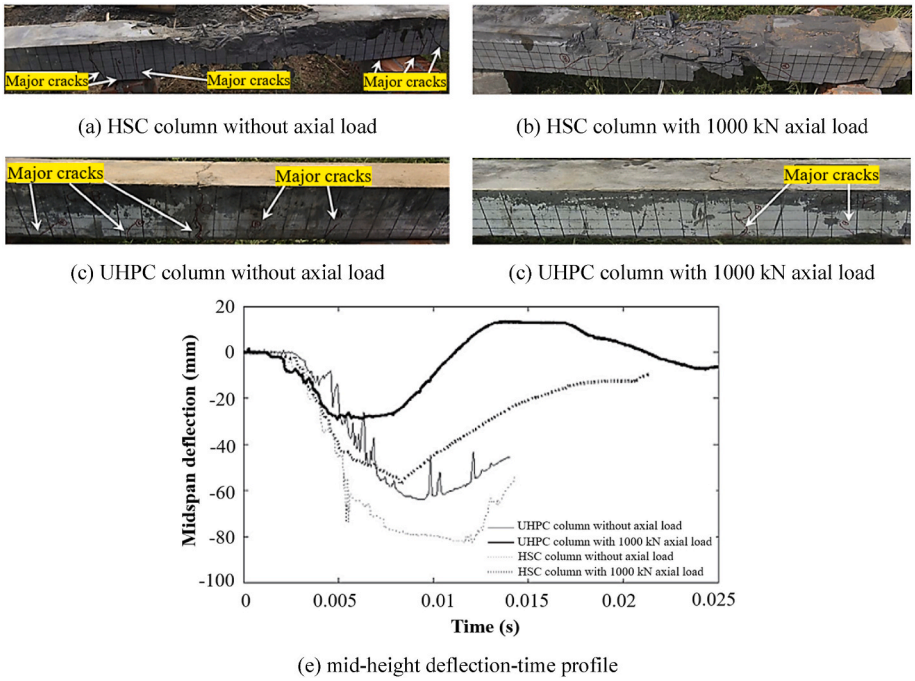

Fig. 26. Comparison of the response of 2500 mm × 200 mm × 200 mm reinforced and fully fixed HSC and UHPC columns to blast loads at $Z = 0.6$ m/kg$^{1/3}$ under free-air busrt environment [82].

transverse reinforcements contributed to reducing the deflection of the UHPC columns. Drawing upon the preceding experimental work, Astarlioglu and Krauthammer [118] extended their investigation using the SDOF model to analyse the behaviour of UHPC columns exposed to four levels of idealised blast loads. The study included a parametric analysis primarily focusing on the effect resulting from the boundary conditions and axial loads. The results indicated that UHPC columns with fixed boundary conditions exhibited nearly half the deflection in comparison to those with simply-supported boundary conditions. Additionally, the application of axial loads spanning from 0 to 2847 kN exerted a beneficial impact on enhancing the blast resistance of the UHPC columns. In a later investigation, Aoude et al. [86] continued employing the ST facility to examine the influence of additional design parameters, such as the longitudinal reinforcement ratio and fibre properties, on the response of UHPC columns to single and repeated blast loads, wherein the test setups and specimen configurations were identical to those employed in Ref. [117]. The findings revealed that higher longitudinal reinforcement ratios and the use of steel fibre with optimised properties, such as increased tensile strength and larger aspect ratio, positively influenced the anti-explosion capacity of UHPC columns. To enhance their analysis, an improved SDOF model that considered partially released boundary effects by incorporating the lumped inelasticity approach was further proposed in their study. This model reasonably predicted the blast response of UHPC columns. However, one assumption made was that the plastic hinge length used in the lumped inelasticity analogy was equal to the effective depth of the UHPC columns. Drawing from experimental observations, it was suggested that the actual plastic hinge length for UHPC columns might be smaller, indicating the need for further investigation into the length effect on blast responses.

To expedite the evaluation of damage to reinforced UHPC columns under blast loads, the use of P-I diagrams is proposed. Given that columns primarily carry axial loads in structures, employing the residual axial load-carrying capacity as the damage criterion proves appropriate for addressing the multiple failure modes experienced by UHPC columns subjected to blast loads [119]. Li et al. [116] proposed a P-I diagram based on the criterion of residual axial load-carrying capacity to quantitatively evaluate the damage of reinforced and fully fixed UHPC columns measuring 2500 mm × 200 mm × 200 mm. These columns were equipped with either straight or twisted steel fibres and subjected to blast loads (17.5–35 kg TNT equivalent) at a standoff distance of 1.5 m (Z = 0.46–0.58 m/kg$^{1/3}$). The damage index D^* was defined as the damage criterion [66], which is given by:

$$D^* = (1 - P_{residual} / P_{max}) \times 100\% \tag{9}$$

where $P_{residual}$ denotes the residual axial load-carrying capacity of the post-blast UHPC column; P_{max} denotes the maximum loading capacity of the undamaged UHPC column. For fitting the P-I diagrams, the equation could be formulated as:

$$(P - P_a)(I - I_a) = \alpha(P_a/2 + I_a/2)^{\beta} \tag{10}$$

where α and β are shape coefficients, dependending on the column configurations and damage degree. In their subsequent research, Li and Wu [120] established a P-I diagram for UHPC columns with twisted steel fibres after accounting for three damage degrees ($D^* = 0.2$, 0.4 and 0.6), revealing specific values for coefficients A and B under each damage degree scenario. For $D^* = 0.2$, the values of A and B were determined as 5.3 and 1.3, respectively. For $D^* = 0.4$, the values of A and B were determined as 5.5 and 1.4, respectively. For $D^* = 0.6$, the values of A and B were determined as 5.5 and 1.35, respectively. A parametric study using the validated numerical model was then carried out to examine the effects of cross-section size (W_c), uniaxial compressive strength of UHPC (f_c), longitudinal reinforcement ratio (ρ) and height (H_c) on the P-I diagram of UHPC columns. Through the least square fitting approach, the pressure and impulse asymptotes were derived as follows:

1) For $D^* = 0.2$:

$$P_a(0.2) = -\frac{0.864H_c}{1000} + 0.0157f_c + \frac{15.4W_c}{1000} + 16.39\rho - 2.1 \tag{11a}$$

$$I_a(0.2) = -\frac{1.05H_c}{1000} + 0.0149f_c + \frac{10.3W_c}{1000} - 1.15\rho + 0.716 \tag{11b}$$

2) For $D^* = 0.4$:

$$P_a(0.4) = -\frac{0.979H_c}{1000} + 0.0189f_c + \frac{20.0W_c}{1000} + 16.89\rho - 2.82 \quad (12a)$$

$$I_a(0.4) = -\frac{0.782H_c}{1000} + 0.0119f_c + \frac{8.18W_c}{1000} + 2.52\rho + 1.47 \quad (12b)$$

3) For $D^* = 0.6$:

$$P_a(0.6) = \exp\left(-\frac{1.06H_c}{1000} + 0.00345f_c + \frac{5.01W_c}{1000} + 6.44\rho + 1.84\right) \quad (13a)$$

$$I_a(0.6) = -\frac{0.551H_c}{1000} + 0.0091f_c + \frac{26.1W_c}{1000} + 7.71\rho - 2.15 \quad (13b)$$

In a more recent study, Rong et al. [121] established an improved P-I diagram to quantitatively evaluate the multiple failure modes of reinforced and fully fixed UHPC columns under blast loads. The construction of the P-I diagram was based on the simplified equivalent SDOF model that incorporated both bending and shear equivalent components. Specifically, the maximum rotating angle at the column end (θ_c) and the average shear strain (γ) were employed as the criteria for failure. The study revealed several key findings. First, the asymptotes of the P-I curves exhibited an upward trend with increasing cross-sectional dimensions, uniaxial compressive strength of UHPC and longitudinal reinforcement ratio. Conversely, a decrease in the slenderness and axial load ratio resulted in a decline in the asymptotic values. The shape of the P-I curves was primarily influenced by the slenderness ratio, axial load ratio and cross-sectional dimensions of the UHPC column.

3. Synergistic use of UHPC with other structures against blast loads

In addition to being directly employed as the structural member, UHPC can be utilised in conjunction with other structures or employed to reinforce existing NRC structures to bolster their resistance to blast loads. The following sections will provide a summary of the anti-explosion performance achieved through the synergistic use of UHPC with other structures, encompassing mesh reinforced UHPC, UHPC-filled steel tubes and UHPC strengthening of NRC structures.

3.1. Mesh reinforced UHPC

In the design of steel reinforcement for UHPC structural members, the usage of HSS rebar is often pursued to achieve a balanced cross-sectional configuration. However, this might lead to increased material cost, and traditional reinforcement fails to fully leverage the workability of UHPC. An alternative to conventional steel rebars is steel wire mesh, which is fabricated with welded grids comprising parallel longitudinal and cross wires set at precise intervals. Concrete reinforced with steel wire mesh, often integrated with self-compacting concrete containing fewer or no coarse aggregates, allows for the creation of a diverse range of structural forms with modifiable performance attributes. The mechanical and physical properties of concrete reinforced with steel wire mesh can be adjusted by modifying the steel grade and volumetric fraction, providing greater flexibility in tailoring the material to specific requirements [122,123].

Li et al. [70] developed an innovative design of high strength self-compacting concrete slab reinforced with steel wire mesh. In this design, the steel wire mesh served as the additional reinforcement within the slab, while steel fibres were incorporated into the concrete mix and employed within the cover layer to offer the micro bridging effect. Medium-field blast tests under the free-air burst circumstance were carried out on the partially fixed one-way slab measuring 2000 mm × 800 mm × 120 mm. The slab was subjected to the 12 kg cylindrical TNT explosive at a standoff distance of 1.5 m (Z = 0.66 m/kg$^{1/3}$). A comparative analysis was also performed with the slab without steel wire mesh reinforcement. As illustrated in Fig. 27, the slab without steel wire mesh exhibited plastic deflection with a plastic hinge along with multiple cracks formed at the slab mid-span. Conversely, under the same blast load, the slab reinforced with steel wire mesh exhibited an elastic response, devoid of permanent deflection, and only hairline cracks were discernible. Notably, these cracks were distributed over a wider area when contrasted with the slab that lacked steel wire mesh reinforcement.

Contact explosion tests conducted by Li et al. [124] using 1 kg cylindrical TNT explosives demonstrated that the additional spall and crater resistance provided by steel wire mesh reinforcement. This enhanced resistance was attributed to the excellent energy absorption capacity and localised tensile membrane effect produced by the steel wire mesh. The closely spaced arrangement of steel wire mesh effectively restricted the propagation of blast waves within the slab, thereby resulting in the reduced perforation and concrete spall. Although the conclusion indicated that augmenting the number of steel wire mesh layers further reduced the slab damage, it remains crucial to address its potential negative implications on the load-carrying capacity and ductility of reinforced concrete. Fig. 28(a)-**(c)** illustrate the corresponding numerical simulations, demonstrating the reduction in slab damage with an increased number of steel wire mesh layers. However, excessive augmentation of these layers could yield detrimental effects. Fig. 28(d) depicts the flexural behaviour of concrete prisms reinforced with 10, 20 and 30 layers of steel wire mesh. The concrete prisms with higher degrees of reinforcement, i.e. 20 layers and 30 layers, failed in a non-ductile shear mode rather than the flexural mode. This phenomenon emerged due to the augmentation in the flexural stiffness outweighing the corresponding increment in the shear capacity. It was observed that heavily concrete prisms would also fail at considerably lower deflections and external forces.

Basalt textile is an alternative mesh reinforcement that can be integrated into concrete to afford corrosion protection, fire resistance and structural strengthening [125–127]. Foglar et al. [106] placed a single layer of basalt textile within the concrete cover between the soffit of the UHPC bridge deck and the underlying steel reinforcement, and then evaluated the near-field blast performance using 25 kg rectangular TNT explosives at a standoff distance of 450 mm (Z = 0.15 m/kg$^{1/3}$). The UHPC bridge deck reinforced with basalt textile experienced more pronounced internal damage as compared to the UHPC bridge deck without basalt textile, whilst the basalt textile contributed to the reinforcement of the anti-explosion behaviour, as evidenced by improvements from the perspective of spalling area and fragment population. In a subsequent investigation conducted by Liu et al. [128], the effects resulting from 20 layers of steel wire mesh and basalt textile on enhancing the resistance of 200 mm thick UHPC slabs with the geopolymer binder to the contact explosion induced by 1 kg rectangular TNT explosives were compared experimentally. The outcomes demonstrated that the steel wire mesh outperformed the basalt textile in maintaining the integrity of the UHPC slab when exposed to contact explosions. This disparity could be ascribed to the inherent brittleness of the basalt textile and the weak interfacial bonding between the basalt textile and UHPC mixture.

3.2. UHPC-filled steel tube

A novel form of steel-concrete composite structure, referred to as concrete-filled steel tube, as well as its variant concrete-filled double steel tubes, has gained popularity within the engineering field in recent decades [129,130]. The concrete-filled steel tube is fabricated by filling concrete into an outer steel tube with a variety of sections, e.g. circular, rectangular, square, etc., while the concrete-filled double steel tubes consists of inner and outer steel tubes with a concentrical arrangement. The key superiority of this composite structure lies in the improved

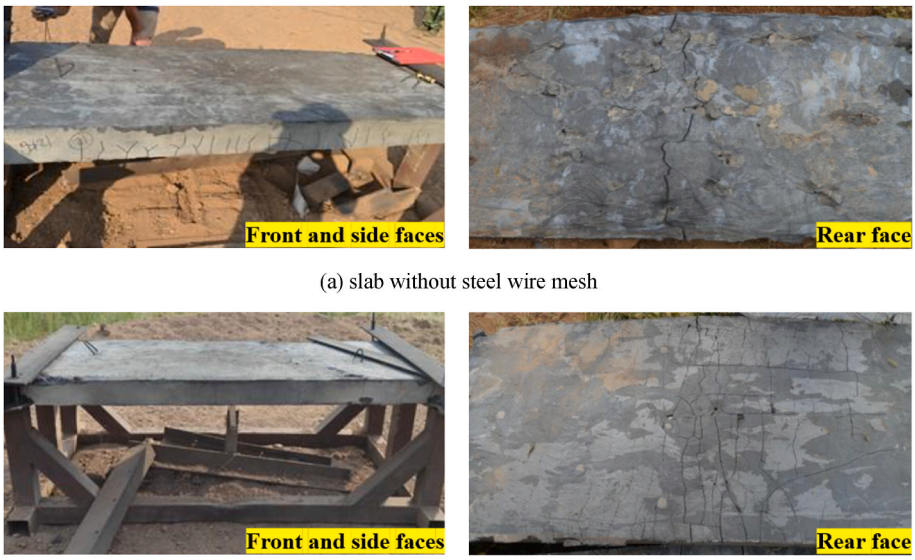

(a) slab without steel wire mesh

(b) slab with steel wire mesh

Fig. 27. Comparison of 2000 mm × 800 mm × 120 mm partially fixed one-way high strength self-compacting concrete slabs with or without steel wire mesh at $Z =$ 0.66 m/kg1/3 under free-air burst environment [70].

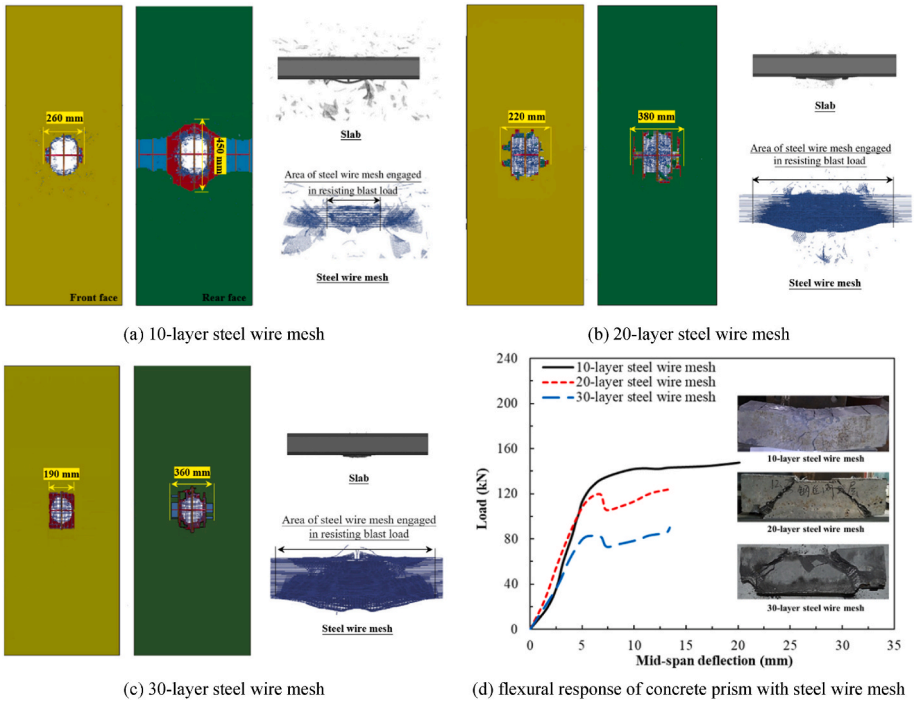

(a) 10-layer steel wire mesh

(b) 20-layer steel wire mesh

(c) 30-layer steel wire mesh

(d) flexural response of concrete prism with steel wire mesh

Fig. 28. Numerical blast and experimental flexural behaviour of concrete specimens with 10, 20 and 30 layers of steel wire mesh [124].

strength and ductility of concrete, facilitated by the confinement effect exerted by the steel tube. Concurrently, the presence of the concrete core provides essential support that can postpone or even prevent local buckling of the steel tube.

Free-air burst experimental investigations (3–10 kg cylindrical TNT explosives at 0.21–0.28 m standoff distance, $Z =$ 0.12–0.14 m/kg$^{1/3}$) have recently been performed by Wu et al. [131] on four fully fixed UHPC-FST columns having dimensions of 203 mm in diameter (6 mm thick steel tube) and 1900 mm in clear length. As presented in Fig. 29, the results indicated that the columns exhibited increasing global deflection and localised damage with the decrease in Z. Su et al. [132] further appraised the near-field explosion performance of bottom fixed UHPC-FST columns with the identical dimensions and properties as those in the earlier investigation [131]. They applied 25 kg cylindrical TNT explosives at various burst heights (0.25 m and 0.95 m) and standoff distances (0.3–0.5 m, Z = 0.1–0.17 m/kg$^{1/3}$) to produce an air burst environment. As depicted in Fig. 30, under a fixed burst height of 0.95 m, the UHPC-FST columns experienced the increasing global deflection and localised damage as Z reduced from 0.17 m/kg$^{1/3}$ to 0.14 m/kg$^{1/3}$, whist they still maintained the structural integrity. When further reducing Z to 0.1 m/kg$^{1/3}$ under a burst height of 0.25 m, the UHPC-FST column responded in a shear failure and completely lost its loading capacity. It was also observed that, under the same Z of 0.14 m/kg$^{1/3}$, the UHPC-FST column suffered less global and localised

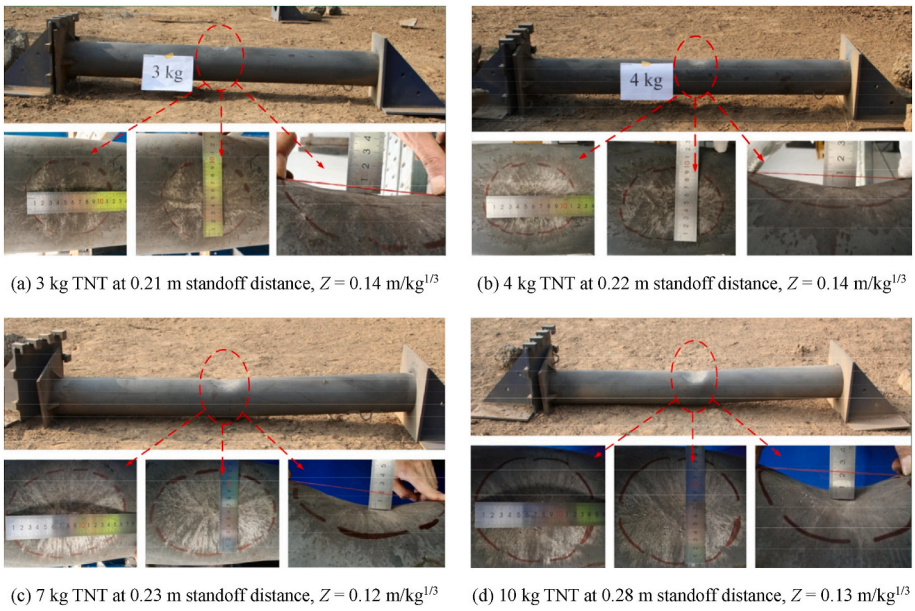

(a) 3 kg TNT at 0.21 m standoff distance, $Z = 0.14$ m/kg$^{1/3}$ (b) 4 kg TNT at 0.22 m standoff distance, $Z = 0.14$ m/kg$^{1/3}$

(c) 7 kg TNT at 0.23 m standoff distance, $Z = 0.12$ m/kg$^{1/3}$ (d) 10 kg TNT at 0.28 m standoff distance, $Z = 0.13$ m/kg$^{1/3}$

Fig. 29. Fully fixed UHPC-FST columns against near-field explosions under free-air bust environment [131].

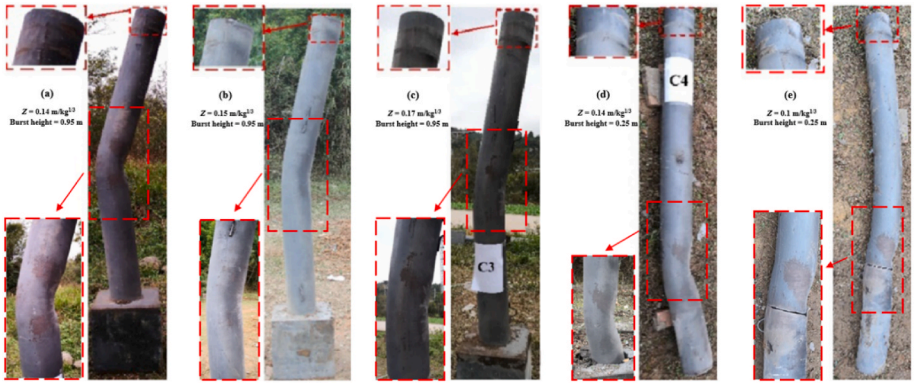

Fig. 30. Bottom fixed UHPC-FST columns against near-field explosions under air bust environment [132].

damage when the burst height shifted from the mid-height (0.95 m) to the bottom of the column (0.25 m). Comparing the UHPC-FST columns with a variety of Z and burst heights, it was concluded that the burst height played a more important role in the global deflection, while Z had a greater effect on the localised damage. Contact explosion behaviour of the same UHPC-FST columns was further examined by Wang et al. [133] through the utilisation of cylindrical TNT explosives with charge weights spanning from 1 kg to 3 kg. In these tests, localised damage was observed around the detonation area without evident global deflection. The severity of the damage escalated proportionally with the TNT charge weight. Subsequent parametric studies based on the validated numerical model revealed that raising the strength grade and thickness of the outer steel tube, the uniaxial compressive strength and sectional dimensions of the core UHPC could enhance the contact explosion tolerance of UHPC-FST columns in terms of the localised damage degree and residual axial capacity [134].

Zhang et al. [135] conducted experimental investigations on UHPC-filled double-steel tube (UHPC-FDST) columns under medium-field blast loading conditions. The columns, with a length of 2500 mm, were subjected to free-air burst tests using cylindrical emulsion explosives with charge weights varying from 24 kg to 70 kg (equivalent to 17.2–50 kg TNT) at a standoff distance of 1.5 m (Z = 0.41–0.58 m/kg$^{1/3}$). Two types of UHPC-FDST columns, including one with both inner and outer tubes circular and the other with both tubes square, were tested. The outer and inner tubes had the diameter/side length of 210 mm and 100 mm, respectively, and the tube thickness was 5 mm. For comparison, two regular UHPC-filled steel tube (UHPC-FST) columns were also included in the test for comparison purpose. The research findings indicated that UHPC-FDST and UHPC-FST columns exhibited similar blast behaviour, with comparable periods of oscillation, maximum and residual mid-height deflections. Raising the amount of explosive charge led to amplified deflections in the UHPC-FDST columns, with this influence being more notable in the case of columns lacking axial loads as opposed to those subjected to axial loading. The presence of the axial load in compression slightly decreased the maximum deflection of UHPC-FDST columns induced by blast loads. Later, with the verified numerical model, Zhang et al. [136] systematically examined the behaviour of UHPC-FDST columns under near-field blast loads influenced by a variety of parameters. Up to a certain threshold, an augmentation in the axial load ratio brought about a slight reduction in the deflection of UHPC-FDST columns. However, once this threshold was surpassed, a substantial rise in the deflection or even structural instability occurred. When the hollow section ratio exceeded 0.5, a considerable increment in the deflection was found, accompanied by a noticeable alteration in the oscillation period. Increasing the thickness of both the inner and outer tubes contributed to smaller deflections, though this effect was more pronounced on the outer tube as compared to the inner tube. The blast loading behaviour of UHPC-FDST

columns was primarily shaped by the configuration of the outer tube, whilst the geometry of the inner tube exhibited a limited impact. Taking into account various design parameters such as square side length (b_s), column height (H_c), axial load ratio (ρ_a), hollow section ratio (ρ_h), steel ratio of the inner tube (ρ_i), steel ratio of the outer tube (ρ_o), uniaxial compressive strength of UHPC (f_c) and yield strength of steel (f_y), P-I diagrams were generated for UHPC-FDST columns against blast loads. The P-I diagrams derived based on the residual axial load-carrying capacity as the damage criterion are presented as follows:

$$(P - P_a)(I - I_a) = 2.2\left(\frac{P_a}{2} + \frac{I_a}{2}\right)^{0.8} \tag{14}$$

The pressure and impulse asymptotes can be expressed by:

$$P_a = 1.364\left(\frac{b_s}{200}\right)^{2.429} + 1.388\left(\frac{H_c}{3500}\right)^{-2.75} - 0.333\left(\frac{\rho_a}{0.3}\right)^2 + 0.24\left(\frac{\rho_a}{0.3}\right) - 0.105\left(\frac{\rho_h}{0.25}\right)^2 + 0.33\left(\frac{\rho_h}{0.25}\right) + 0.188\left(\frac{\rho_i}{0.07}\right) + 0.763\left(\frac{\rho_o}{0.128}\right) + 0.567\left(\frac{f_c}{170}\right) + 0.831\left(\frac{f_y}{350}\right) - 3.863 \tag{15a}$$

$$I_a = 10.972\left(\frac{b_s}{200}\right)^{1.283} + 10.133\left(\frac{H_c}{3500}\right)^{-0.935} - 1.591\left(\frac{\rho_a}{0.3}\right)^2 + 2.143\left(\frac{\rho_a}{0.3}\right) - 2.112\left(\frac{\rho_h}{0.25}\right)^2 + 2.561\left(\frac{\rho_h}{0.25}\right) + 1.564\left(\frac{\rho_i}{0.07}\right) + 6.456\left(\frac{\rho_o}{0.128}\right) + 1.7\left(\frac{f_c}{170}\right) + 3.562\left(\frac{f_y}{350}\right) - 24.7 \tag{15b}$$

To facilitate comparison, the P-I curves generated using Eq. (14) are plotted in Fig. 31 together with the numerically computed data points. It was found that the numerically determined data points fairly aligned with the fitted curves established using the suggested analytical equation.

3.3. UHPC strengthening of NRC structures

Enhancing the anti-explosion performance of existing NRC structures is an emerging and significant area worthy of attention. Besides increasing the inherent strength, ductility and toughness of concrete, another effective way involves utilising UHPC as an additional overlay [137–140] or retrofitting layer (replacing part of the concrete cover) [141–144] upon the existing NRC structures. This can be achieved through various strengthening approaches, such as reinforcing the compression or tension side, lateral side, U-shape, or full sides, employing either cast-in-place or prefabricated technique for construction. The adoption of UHPC for strengthening purposes helps hinder potential drawbacks associated with other strengthening technologies, such as steel jacketing and fibre reinforced polymer (FRP) wrapping. Notably, UHPC addresses issues like fire resistance, corrosion, and debonding encountered in steel jacketing [145,146], as well as the bonding material degradation at the interface in FRP wrapping [147].

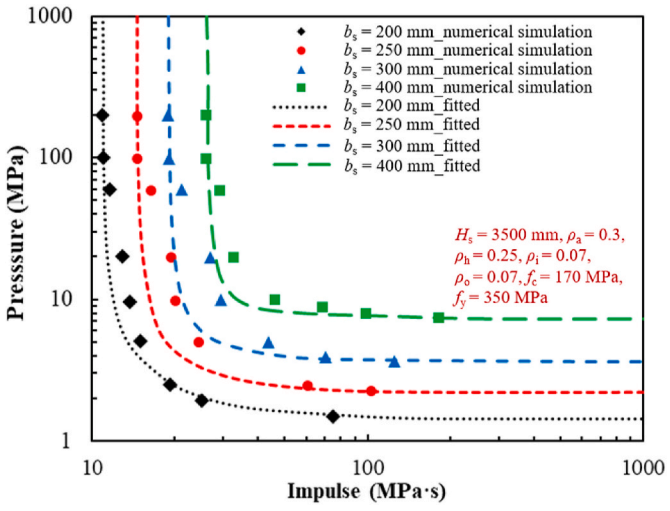

Fig. 31. Numerically calculated P-I data points for various magnitudes of b_s [136].

Ma et al. [148] applied 20–80 mm thick 3D printed UHPC layer snugly onto the compression side of NRC slabs with a fixed total thickness of 150 m, and assessed their contact explosion resistance using 0.4 kg rectangular TNT explosives. It was noted that the extent of localised damage, including crater formation and scabbing, did not consistently follow an increasing or decreasing trend with the augmentation of UHPC layer thickness. This inconsistency in the damage behavior could be attributed to the complex interaction between the incident and reflected stress waves at the interface between the UHPC layer and NRC slab, as well as the diffractive stress waves resulting from the heterogeneous material composition.

Li and Aoude [149] applied the ST facility to assess the dynamic response of three 2440 mm × 150 mm × 200 mm simply-supported NRC beams retrofitted with 20 mm thick UHPC layers on all sides over the span (referred as UHPC-F-NRC), under single and consecutive reflected impulse loads. Fig. 32 presents a comparison between NRC and UHPC-F-NRC beams subjected to a single reflected impulse load of approximately 0.38 MPa ms. The UHPC-F-NRC beam exhibited significant improvements as compared to the NRC beam, including a reduction of approximately 40 % in support rotation, maximum and residual mid-span deflections. The UHPC-F-NRC beam also effectively mitigated spalling damage, as evidenced by the presence of a major crack accompanied by several hairline cracks, without causing steel rebar fracture. Furthermore, the UHPC-F-NRC beam demonstrated superior residual capacity and stiffness after the blast, though its residual ductility was slightly lower than that of the NRC beam. Three consecutive reflected impulse loads roughly varying from 0.14 MPa ms to 0.38 MPa ms were also acted on the NRC and UHPC-F-NRC beams in this study to compare their blast performance. Under the first two blast events, the UHPC-F-NRC beam outperformed the NRC beam concerning the support rotation, maximum and residual mid-span deflections. Although an evident steel rebar fracture occurred in the UHPC-F-NRC beam under the third blast event, the retrofitting UHPC layer exhibited the superiority in suppressing the generation of concrete debris. Subsequent to the validation of the numerical model, additional parametric investigations were conducted, revealing that increasing the longitudinal reinforcement ratio and UHPC layer thickness contributed to reduced mid-span deflections, support rotations and damage degree in the UHPC retrofitted NRC beams under both single and consecutive blast loads. Additionally, slightly enlarging the distance between the UHPC layer interface and the longitudinal reinforcement was capable of protecting the steel rebar from fracture.

Subsequently, Li and Aoude [150] probed into the effects of different UHPC retrofitting configurations on the single and consecutive blast behaviour of 2440 mm × 150 mm × 200 mm simply-supported NRC beams, using the same test conditions as their previous research [149]. Fig. 33 presents the anti-explosion performance of three UHPC retrofitting configurations applied to NRC beams, including UHPC-F-NRC (full retrofitting over the span), UHPC-F(H)-NRC (full retrofitting in the middle hinge region) and UHPC-T-F(H)-NRC (retrofitting on the tension side over the span and full retrofitting in the middle hinge region) under a single reflected impulse load of approximately 0.38 MPa ms. The

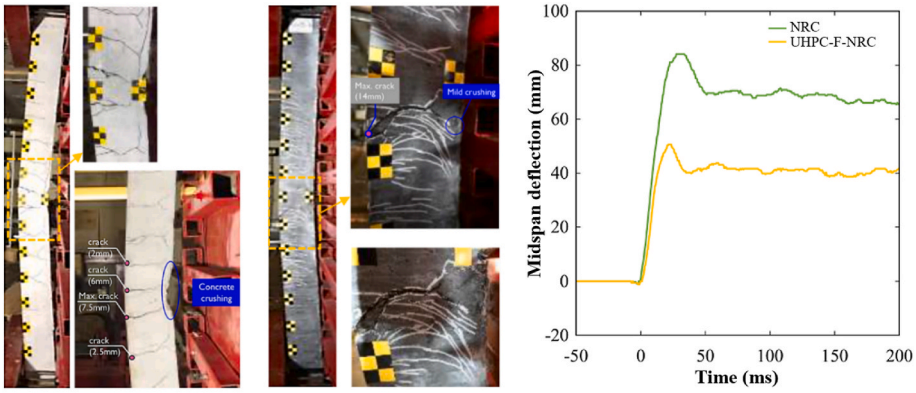

(a) NRC (b) UHPC-FS-NRC (c) mid-span deflection

Fig. 32. Comparison of the response of simply-supported NRC and UHPC-FS-NRC beams under the single reflected impulse of ~0.38 MPa ms [149].

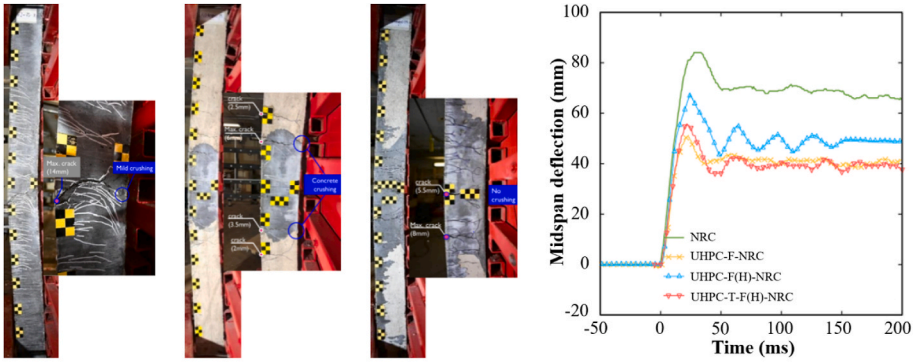

(a) UHPC-F-NRC (b) UHPC-F(H)-NRC (c) UHPC-T-F(H)-NRC (d) mid-span deflection

Fig. 33. Influences of UHPC retrofitting configurations on the blast behaviour of simply-supported NRC beams under the single reflected impulse of ~0.38 MPa ms [150].

results revealed that full retrofitting over the span yielded the most pronounced reduction in the maximum mid-span deflection of the NRC beam, followed by a hybrid approach of tension side retrofitting over the span and full retrofitting in the middle hinge region, and the approach of full retrofitting in the middle hinge region alone. Additionally, all three retrofitted NRC beams demonstrated improved post-blast capacity as compared to the NRC beam, with UHPC-F-NRC and UHPC-T-F(H)-NRC exhibiting superior stiffness and strength. The study also investigated the blast resistance of the three UHPC retrofitting configurations under three consecutive blast loads, with reflected impulse loads of 0.14–0.38 MPa ms. Three UHPC retrofitting configurations over the span, including tension side retrofitting, U-shape retrofitting (tension side and two lateral sides) and full retrofitting, were designed to comparatively investigate their anti-explosion capacity. The U-shape retrofitting approach showed the optimal performance in decreasing the maximum mid-span deflection of the NRC beam, especially under the first two blast loads. However, all three retrofitting approaches responded with failure due to the steel rebar fracture under the third blast load. Leveraging the verified numerical model, parametric investigations were further conducted to draw a conclusion that improving the longitudinal reinforcement ratio resulted in additional reductions in mid-span deflections for UHPC-retrofitted NRC beams. This adjustment also contributed to the postponement or prevention of steel bar rupture, evident under both single and consecutive blast loads.

The resistance of NRC columns strengthened by UHPC to blast loads was also investigated by Lee et al. [151] using the ST facility. In their research, a 15 mm thick UHPC layer was applied to fully retrofit a partially fixed NRC column measuring 2468 mm × 160 mm × 160 mm. The column was subjected to three repeated reflected impulse loads ranging approximately from 0.1 MPa ms to 0.5 MPa ms. The UHPC retrofitting contributed to an evident enhancement in the explosion tolerance of the NRC column, resulting in decreased maximum and residual mid-height deflections. Furthermore, the UHPC retrofitting technique effectively suppressed the crack distribution caused by the blast load on the column. Similarly, Wang et al. [152] numerically verified the superiority of NRC columns fully retrofitted with an 80 mm thick UHPC layer against blast loads. Through the comparative analysis and parametric studies, key design parameters for enhancing the blast resistance of retrofitted NRC columns are identified. Overall, under the air burst loading condition with Z = 0.12–1.39 m/kg$^{1/3}$, both the maximum deflection and damage degree of UHPC retrofitted NRC columns were lower than those of NRC columns. The longitudinal reinforcement ratio and UHPC retrofitting length were two priority factors for improving the blast resistance, while the UHPC retrofitting layer thickness had the most substantial impact on strengthening the post-blast capacity of the columns.

4. Concluding remarks and recommendations for future research work

This paper provides an exhaustive overview of the existing experimental, numerical and theoretical research on the behavior of UHPC structural elements, including slabs, beams and columns, as well as UHPC-based composite structures like mesh-reinforced UHPC, UHPC-filled steel tubes and UHPC strengthening of NRC structures, under blast loading conditions. Upon a thorough review and extensive discussions, the following conclusions are deduced:

1) Owing to the exceptional strength, ductility, energy absorption capacity and damage tolerance, UHPC structural members outperform NRC and HSC counterparts in resisting blast loads. They excel in restraining structural responses, minimising localised damage, controlling crack propagation and reducing fragmentation under various blast loading conditions.
2) Increasing the steel reinforcement ratio within a certain range enhances the performance of UHPC slabs in close- and medium-field explosions. However, its effect on localised damage is minimal under contact explosions. Steel fibre parameters like geometry, strength and content boost blast performance of UHPC slabs, with fibre length slightly affecting blast resistance. The positive effect of steel fibre content is more pronounced in medium-field explosions than far-field explosions. Both slab thickness and blast scaled distance are important factors that influence the failure mode of UHPC slabs against blast loads.
3) Utilising support rotation and average shear strain as the respective flexural and shear failure criteria, an improved P-I diagram is proposed for one-way UHPC slabs. This diagram considers various factors including slab span, thickness, longitudinal reinforcement ratio, UHPC compressive strength, load level and boundary condition that influence the asymptotes. Empirical models considering the slab thickness and TNT equivalent are validated to evaluate the localised damage of UHPC slabs exposed to contact explosions.
4) GFRP rebars exhibit evident advantages over HSS rebars in enhancing the blast tolerance of UHPC beams, resulting in substantial rebound deflection and minimised residual deflection. The combination of compressive and tensile longitudinal reinforcements, along with transverse reinforcement, reduces deflection and localised damage. For UHPC beams with HSS rebars, increasing the steel fibre content improves blast resistance until reaching a threshold, beyond which blast resistance decreases. Using shorter steel fibres with a larger aspect ratio effectively improves the blast capacity of UHPC beams.
5) Increasing the axial load level and employing fully fixed boundary conditions, along with reducing the spacing of transverse reinforcements, effectively restrain the structural response of UHPC columns against blast loads. Moreover, enlarging the steel fibre and reinforcement contents within a certain threshold, along with improving the steel fibre strength and aspect ratio, positively enhances the anti-explosion capacity of UHPC columns.
6) Employing the residual loading capacity as the damage criterion, an improved P-I diagram for UHPC columns has been established. This diagram considers the influence of factors such as cross-sectional size, uniaxial compressive strength of UHPC, longitudinal reinforcement ratio and height on the asymptotes. Utilising the maximum rotating angle at the column end and the average shear strain as the respective criteria for flexural and shear failure, another updated P-I diagram is proposed for UHPC columns. This diagram highlights the effect of the axial load ratio on the asymptotes.
7) When the UHPC structural member is reinforced with steel rebars, it tends to experience strain concentration, leading to concentrated large cracks and subsequent failure at mid-span, also resulting in wastage of the remaining UHPC material. In comparison to NRC, the ductility of UHPC structural members may decrease.
8) Compared to basalt textile, steel wire mesh reinforcement presents superior performance in improving the blast resistance of UHPC slabs. While augmenting the number of steel wire mesh layers helps reduce slab damage, it is essential to consider its potential adverse impacts on the load-carrying capacity and ductility of UHPC slabs.
9) UHPC-filled steel tubes exhibit excellent blast resistance, particularly under near-field and contact explosions. Both UHPC-FDST and UHPC-FST columns exhibit similar blast behaviour, with increased outer tube thickness and steel strength grade proving more effective in enhancing blast resistance. A P-I diagram is established for UHPC-FDST columns, using the residual loading capacity as the damage criterion. This diagram considers factors such as square side length, column height, axial load ratio, hollow section ratio, steel ratio of the inner tube, steel ratio of the outer tube, uniaxial compressive strength of UHPC and yield strength of steel.
10) Retrofitting NRC structural members with a UHPC layer proves effective in enhancing blast resistance. The UHPC retrofitting layer thickness has the most significant impact on strengthening blast performance. Among the retrofitting strategies, both U-shape retrofitting and a hybrid approach, involving retrofitting on the tension side over the span and full retrofitting in the middle hinge region, demonstrate optimal performance in mitigating structural damage under blast loads.
11) The closed or patented nature of formulas and mixing methods of UHPC hinders its further development and optimisation. Meanwhile, the non-uniformity in UHPC compositions leads to notable variations in mechanical properties, contributing to disparities in the blast-resistant performance. Therefore, the open-recipe UHPC as proposed by El-Tawil et al. [153] deserves promotion, as its open development will encourage future innovations, significantly reduce the cost of raw materials and contribute to widespread applications in protective structures as well as other fields.

In recent years, there has been a prosperous advancement in material science, leading to the emergence of geopolymer as a promising binder. Geopolymers, typically synthesised using slag, fly ash and other aluminosilicate materials, offer an promising alternative to Portland cement, providing potential cost-effectiveness and sustainability while maintaining high mechanical properties. Although some studies have explored the dynamic response of geopolymer-based UHPC (G-UHPC) to blast loads, more research is needed for a comprehensive understanding of its properties before wider applications, especially for blast resistance design. Future research might focus on investigating the mechanical behaviour of G-UHPC under complex stress states and dynamic loading conditions to improve the comprehension of this material. Additionally, experimental investigations are essential to explore the performance of G-UHPC structural members under various blast scenarios. Complementing physical tests, numerical models using both homogeneous and heterogeneous approaches can offer valuable insights into the response of G-UHPC structural members to blast loads. Before that, the establishment of an accurate concrete constitutive model specifically tailored to accommodate the dynamic characteristics of G-UHPC is a prerequisite for advancing the numerical simulations.

3D printing technology is in the future to play a pivotal role in the future blast design of UHPC structural members. By harnessing 3D printing techniques, intricate and complex geometries can be created, tailoring UHPC structural members to withstand specific blast loading conditions. Custom-designed components using 3D printing enable optimising structural integrity and blast resistance, resulting in enhanced safety and performance. Moreover, 3D printing techniques enable the ideal incorporation of advanced materials, such as fibers or nanomaterials, into UHPC structural members, further augmenting their blast-resistant properties with superior strength, ductility and energy absorption capacity. The 3D printing technology also facilitates rapid prototyping and iterative design processes, enabling efficient testing and refining of various UHPC structural member configurations for blast resistance.

Machine learning is a promising and powerful tool for analysing the blast behaviour of UHPC structural members. Its key advantage lies in handling complex and non-linear relationships between parameters and

blast performance outcomes. Additionally, machine learning enables the assessment of factors affecting blast resistance, helping prioritise critical design considerations for more efficient design processes and improved blast-resistant UHPC structures. Machine learning models can be trained using experimental and numerical data to learn the behavior of UHPC structural members under different blast scenarios. These models can then predict the blast resistance of various UHPC configurations, optimising design parameters for enhanced performance and safety.

CRediT authorship contribution statement

Jian Liu: Conceptualization, Data curation, Formal analysis, Investigation, Methodology, Writing – original draft. **Jie Wei:** Data curation, Formal analysis, Investigation. **Jun Li:** Methodology, Writing – review & editing. **Yu Su:** Conceptualization, Formal analysis. **Chengqing Wu:** Conceptualization, Funding acquisition, Investigation, Methodology, Supervision, Writing – review & editing.

Declaration of competing interest

We wish to confirm that there are no known conflicts of interest associated with this publication and there has been no significant financial support for this work that could have influenced its outcome.

We confirm that the manuscript has been read and approved by all named authors and that there are no other persons who satisfied the criteria for authorship but are not listed. We further confirm that the order of authors listed in the manuscript has been approved by all of us.

We confirm that we have given due consideration to the protection of intellectual property associated with this work and that there are no impediments to publication, including the timing of publication, with respect to intellectual property. In doing so we confirm that we have followed the regulations of our institutions concerning intellectual property.

We understand that the Corresponding Author is the sole contact for the Editorial process (including Editorial Manager and direct communications with the office). He is responsible for communicating with the other authors about progress, submissions of revisions and final approval of proofs. We confirm that we have provided a current, correct email address which is accessible by the Corresponding Author and which has been configured to accept email from chengqing.wu@uts.edu.au.

Data availability

Data will be made available on request.

Acknowledgement

The authors would like to express sincere gratitude for the financial support extended by the National Natural Science Foundation of China (Grant No. 51908148) and the Science and Technology Program of Guangzhou (Grant No. 2024A03J0390), which greatly facilitated the execution of this research.

Appendix

Table 1
Summary of investigations on UHPC slabs under blast loads

Refs.	f_c (MPa)	Methods	Blast scenarios	Investigated parameters	Indexes
[101]	164.2	Experimental (FB)	Hexoline; Surface burst; Far-field	Concrete type Blast scaled distance, Z	Mid-span deflection Damage mode and crack distribution
[102,154]	170–190	Experimental (FB) Numerical (CONWEP)	TNT; Air burst; Far-field	Effectiveness of tensile longitudinal reinforcement Effectiveness of steel fibres	Mid-span deflection Damage mode and crack distribution
[103]	158	Numerical (CONWEP)	TNT; Air burst; Medium- and far-field	Slab thickness Blast scaled distance, Z Tensile longitudinal reinforcement ratio	Mid-span deflection Damage mode
[104,110]	151.6	Experimental (FB) Numerical (CONWEP)	Composition B; Free-air burst; Medium-field	Effectiveness of tensile longitudinal reinforcement	Mid-span deflection Damage mode and crack distribution Energy absorption
[62]	128.9	Experimental (FB) Numerical (CONWEP)	Composition B; Free-air burst; Medium- and far-field	Concrete type Blast scaled distance, Z Tensile longitudinal reinforcement strength and ratio	Mid-span deflection Damage mode and crack distribution
[105]	128.9	Numerical (CONWEP)	TNT; Free-air burst; Medium- and far-field	Concrete type Blast scaled distance, Z Tensile longitudinal reinforcement ratio	Mid-span deflection
[54,155]	125.3	Experimental (FB) Numerical (CONWEP)	TNT; Free-air burst; Medium-field	Concrete type Blast scaled distance, Z	Mid-span deflection Slab vibration Damage mode and crack distribution
[87]	201	Experimental (BS) Numerical (ITI)	Free-air burst; Far-field	Magnitude of impulse load Tensile strength of UHPC Dissipated energy density	Mid-span deflection Critical impulse for slab fracture
[106]	125.8–129.5	Experimental (FB) Numerical (CONWEP)	TNT; Free-air burst; Near-field	Concrete type Steel fibre length and content	Mid-span deflection Damage mode and crack distribution
[107,156]	202.9	Experimental (FB) Numerical (CONWEP)	ANFO; Free-air burst; Medium-field	Concrete type Effectiveness of tensile longitudinal reinforcement Effectiveness of steel fibres	Mid-span deflection Damage mode and crack distribution Steel rebar and concrete strain Slab vibration
[108]	170–200	Experimental (FB)	PE4; Free-air burst; Medium-field	Blast scaled distance, Z	1/4 span deflection

(*continued on next page*)

Table 1 (*continued*)

Refs.	f_c (MPa)	Methods	Blast scenarios	Investigated parameters	Indexes
		Numerical (CONWEP)		Steel fibre length and content	Damage mode and crack distribution
[109]	175	Theoretical (FD)	Composition B; Free-air burst; Medium-field	Slab span and thickness	P-I diagram
[78]	100–200	Theoretical (SDOF)	TNT; Free-air burst; Near-, medium- and far-field	Slab span and thickness Tensile longitudinal reinforcement ratio Uniaxial compressive strength of UHPC Boundary condition Load level	P-I diagram
[71,110, 113,157]	145	Experimental (FB) Numerical (SPH) Numerical (ALE)	TNT; Free-air burst; Contact	Concrete type Tensile longitudinal reinforcement ratio TNT charge weight Slab thickness	Damage mode and crack distribution Steel rebar strain Concrete debris distribution model Localised damage degree model
[112]	180	Experimental (FB) Numerical (ALE)	TNT; Free-air burst; Contact	TNT charge weight Slab thickness	Damage mode and crack distribution
[114]	90–104	Experimental (FB) Numerical (ALE)	TNT; Free-air burst; Contact	Concrete type Effectiveness of steel fibres Fibre type TNT charge weight Slab thickness	Damage mode and crack distribution Localised damage degree model

Table 2
Summary of investigations on UHPC beams under blast loads

Refs.	f_c (MPa)	Methods	Blast scenarios	Investigated parameters	Indexes
[83]	121	Experimental (FB) Numerical (ALE)	TNT; Free-air burst; Near-field	Concrete type Tensile longitudinal reinforcement type and ratio Effectiveness of transverse reinforcement Effectiveness of compressive reinforcement	Mid-span deflection Damage mode and crack distribution Energy absorption Axial stress at mid-span Reaction force
[88]	115–156	Experimental (ST) Theoretical (SDOF)	Free-air burst; Far-field	Concrete type Steel fibre type and content Tensile longitudinal reinforcement strength and ratio Effectiveness of transverse reinforcement	Mid-span deflection Damage mode and crack distribution Maximum support rotation
[115]	116.1	Machine-learning	Free-air burst; Far-field	Concrete type Tensile longitudinal reinforcement strength Steel fibre length and content	Mid-span deflection

Table 3
Summary of investigations on UHPC columns under blast loads

Refs.	f_c (MPa)	Methods	Blast scenarios	Major investigated parameters	Indexes
[82, 158]	148	Experimental (FB) Numerical (CONWEP)	Emulsion; Free-air burst; Medium- and far-field	Concrete type Blast scaled distance, Z Compressive axial load	Mid-height deflection Damage mode and crack distribution
[117]	144.7–165.4	Experimental (ST) Theoretical (SDOF)	Free-air burst; Far-field	Concrete type Steel fibre content Transverse reinforcement spacing	Mid-height deflection Damage mode and crack distribution Steel rebar strain Support rotation Blast fragment
[118]	164.1	Numerical (ITI) Theoretical (SDOF)	Free-air burst; Far-field	Concrete type Boundary condition Compressive axial load level	Mid-height deflection P-I diagram
[86]	128–165	Experimental (ST) Theoretical (SDOF)	Free-air burst; Far-field	Concrete type Steel fibre type and content Tensile longitudinal reinforcement ratio Transverse reinforcement spacing	Mid-height deflection Damage mode and crack distribution
[116]	130–148	Experimental (FB)	Emulsion; Free-air burst; Medium-field	Steel fibre type Blast scaled distance, Z Compressive axial load level	Damage mode and crack distribution Residual loading capacity P-I diagram
[120]	127–160	Numerical (CONWEP)	TNT; Free-air burst; Medium-field	Cross-sectional dimensions Uniaxial compressive strength of UHPC	Damage mode and crack distribution

(*continued on next page*)

Table 3 (*continued*)

Refs.	f_c (MPa)	Methods	Blast scenarios	Major investigated parameters	Indexes
[121]	90–210	Theoretical (SDOF)	TNT; Free-air burst; Medium-field	Tensile longitudinal reinforcement ratio Column height Slenderness ratio Cross-sectional dimensions Tensile longitudinal reinforcement ratio Uniaxial compressive strength of UHPC Compressive axial load level	Residual loading capacity P-I diagram P-I diagram

References

[1] P. Richard, M. Cheyrezy, Composition of reactive powder concretes, Cement Concr. Res. 25 (1995) 1501–1511.
[2] O.V. Aleksandrova, N.D.V. Quang, B.I. Bulgakov, S.V. Fedosov, N.A. Lukyanova, V.B. Petropavlovskaya, The effect of mineral admixtures and fine aggregates on the characteristics of high-strength fiber-reinforced concrete, Materials 15 (2022) 8851.
[3] F. Alhussainy, H.A. Hasan, M.N. Sheikh, M.N. Hadi, A New Method for Direct Tensile Testing of Concrete, 2019.
[4] LÁd Oliveira Júnior, VEdS. Borges, A.R. Danin, D.V.R. Machado, DdL. Araújo, M. K. El Debs, P.F. Rodrigues, Stress-strain curves for steel fiber-reinforced concrete in compression, Materia 15 (2010) 260–266.
[5] E.A. Schauffert, G. Cusatis, D. Pelessone, J.L. O'Daniel, J.T. Baylot, Lattice discrete particle model for fiber-reinforced concrete. II: tensile fracture and multiaxial loading behavior, J. Eng. Mech. 138 (2012) 834–841.
[6] S. Xu, P. Wu, C. Wu, Calibration of KCC concrete model for UHPC against low-velocity impact, Int. J. Impact Eng. 144 (2020) 103648.
[7] D.-Y. Yoo, N. Banthia, Mechanical properties of ultra-high-performance fiber-reinforced concrete: a review, Cement Concr. Compos. 73 (2016) 267–280.
[8] D.-Y. Yoo, N. Banthia, Impact resistance of fiber-reinforced concrete-A review, Cement Concr. Compos. 104 (2019) 103389.
[9] X. Chen, S. Wu, J. Zhou, Compressive strength of concrete cores under high strain rates, J. Perform. Constr. Facil. 29 (2015) 06014005.
[10] D. Yan, G. Lin, Dynamic properties of concrete in direct tension, Cement Concr. Res. 36 (2006) 1371–1378.
[11] K. Fujikake, T. Senga, N. Ueda, T. Ohno, M. Katagiri, Nonlinear analysis for reactive powder concrete beams under rapid flexural loadings, J. Adv. Concr. Technol. 4 (2006) 85–97.
[12] L.J. Malvar, J.E. Crawford, Dynamic increase factors for concrete, DTIC document 1 (1998) 1–6.
[13] J. Du, W. Meng, K.H. Khayat, Y. Bao, P. Guo, Z. Lyu, A. Abu-Obeidah, H. Nassif, H. Wang, New development of ultra-high-performance concrete (UHPC), Compos. B Eng. 224 (2021) 109220.
[14] C. Shi, Z. Wu, J. Xiao, D. Wang, Z. Huang, Z. Fang, A review on ultra high performance concrete: Part I. Raw materials and mixture design, Construct. Build. Mater. 101 (2015) 741–751.
[15] S.M. Qaidi, D.S. Atrushi, A.S. Mohammed, H.U. Ahmed, R.H. Faraj, W. Emad, B. A. Tayeh, H.M. Najm, Ultra-high-performance geopolymer concrete: a review, Construct. Build. Mater. 346 (2022) 128495.
[16] H. Huang, X. Gao, L. Teng, Fiber alignment and its effect on mechanical properties of UHPC: an overview, Construct. Build. Mater. 296 (2021) 123741.
[17] I.L. Larsen, R.T. Thorstensen, The influence of steel fibres on compressive and tensile strength of ultra high performance concrete: a review, Construct. Build. Mater. 256 (2020) 119459.
[18] J. Gong, Y. Ma, J. Fu, J. Hu, X. Ouyang, Z. Zhang, H. Wang, Utilization of fibers in ultra-high performance concrete: a review, Compos. B Eng. 241 (2022) 109995.
[19] D.-Y. Yoo, N. Banthia, Y.-S. Yoon, Recent development of innovative steel fibers for ultra-high-performance concrete (UHPC): a critical review, Cement Concr. Compos. (2023) 105359.
[20] D.-Y. Yoo, T. Oh, N. Banthia, Nanomaterials in ultra-high-performance concrete (UHPC)–A review, Cement Concr. Compos. (2022) 104730.
[21] L. Lei, T. Hirata, J. Plank, 40 years of PCE superplasticizers-History, current state-of-the-art and an outlook, Cement Concr. Res. 157 (2022) 106826.
[22] M.T. Marvila, A.R.G. de Azevedo, P.R. de Matos, S.N. Monteiro, C.M.F. Vieira, Materials for production of high and ultra-high performance concrete: review and perspective of possible novel materials, Materials 14 (2021) 4304.
[23] D. Fan, J. Zhu, M. Fan, J.-X. Lu, S. Chu, E. Dong, R. Yu, Intelligent design and manufacturing of ultra-high performance concrete (UHPC)-A review, Construct. Build. Mater. 385 (2023) 131495.
[24] S. Wang, B. Wang, H. Zhu, G. Chen, Z. Li, L. Yang, Y. Zhang, X. Zhou, Ultra-high performance concrete: mix design, raw materials and curing regimes-A Review, Mater. Today Commun. (2023) 105468.
[25] M. Zhou, Z. Wu, X. Ouyang, X. Hu, C. Shi, Mixture design methods for ultra-high-performance concrete-a review, Cement Concr. Compos. 124 (2021) 104242.
[26] D. Xu, J. Tang, X. Hu, C. Yu, F. Han, S. Sun, W. Deng, J. Liu, The influence of curing regimes on hydration, microstructure and compressive strength of ultra-high performance concrete: a review, J. Build. Eng. (2023) 107401.
[27] H. Hamada, A. Alattar, B. Tayeh, F. Yahaya, I. Almeshal, Influence of different curing methods on the compressive strength of ultra-high-performance concrete: a comprehensive review, Case Stud. Constr. Mater. (2022) e01390.
[28] S. Ahmed, Z. Al-Dawood, F. Abed, M.A. Mannan, M. Al-Samarai, Impact of using different materials, curing regimes, and mixing procedures on compressive strength of reactive powder concrete-A review, J. Build. Eng. 44 (2021) 103238.
[29] Y. Zhu, H. Hussein, A. Kumar, G. Chen, A review: material and structural properties of UHPC at elevated temperatures or fire conditions, Cement Concr. Compos. 123 (2021) 104212.
[30] R.J. Thomas, A.D. Sorensen, Review of strain rate effects for UHPC in tension, Construct. Build. Mater. 153 (2017) 846–856.
[31] D. Wang, C. Shi, Z. Wu, J. Xiao, Z. Huang, Z. Fang, A review on ultra high performance concrete: Part II. Hydration, microstructure and properties, Construct. Build. Mater. 96 (2015) 368–377.
[32] Y. Huang, J. Wang, H. Shang, X. Liu, Creep behaviour of ultra-high-performance concrete (UHPC): a review, J. Build. Eng. (2023) 106187.
[33] L. Yang, C. Shi, Z. Wu, Mitigation techniques for autogenous shrinkage of ultra-high-performance concrete-A review, Compos. B Eng. 178 (2019) 107456.
[34] H. Wu, A. Shen, Y. Cai, Q. Ma, G. Ren, S. Deng, H. Pan, Interfacial bond properties and pullout behaviors of steel fibers embedded in ultra-high-performance concrete: a review, Mater. Today Commun. (2023) 106081.
[35] K.H. Khayat, W. Meng, K. Vallurupalli, L. Teng, Rheological properties of ultra-high-performance concrete-An overview, Cement Concr. Res. 124 (2019) 105828.
[36] Y. Deng, Z. Zhang, C. Shi, Z. Wu, C. Zhang, Steel Fiber-Matrix Interfacial Bond in Ultra-high Performance Concrete: A Review, Engineering, 2022.
[37] M. Amran, S.-S. Huang, A.M. Onaizi, N. Makul, H.S. Abdelgader, T. Ozbakkaloglu, Recent trends in ultra-high performance concrete (UHPC): current status, challenges, and future prospects, Construct. Build. Mater. 352 (2022) 129029.
[38] J. Liu, J. Li, J. Fang, Y. Su, C. Wu, Ultra-high performance concrete targets against high velocity projectile impact–a-state-of-the-art review, Int. J. Impact Eng. 160 (2022) 104080.
[39] D.-Y. Yoo, N. Banthia, Mechanical and structural behaviors of ultra-high-performance fiber-reinforced concrete subjected to impact and blast, Construct. Build. Mater. 149 (2017) 416–431.
[40] J. Xue, B. Briseghella, F. Huang, C. Nuti, H. Tabatabai, B. Chen, Review of ultra-high performance concrete and its application in bridge engineering, Construct. Build. Mater. 260 (2020) 119844.
[41] M. Zhou, W. Lu, J. Song, G.C. Lee, Application of ultra-high performance concrete in bridge engineering, Construct. Build. Mater. 186 (2018) 1256–1267.
[42] M. Elmorsy, W. Hassan, Seismic behavior of ultra-high performance concrete elements: state-of-the-art review and test database and trends, J. Build. Eng. 40 (2021) 102572.
[43] Y. Zhu, Y. Zhang, H.H. Hussein, G. Chen, Flexural strengthening of reinforced concrete beams or slabs using ultra-high performance concrete (UHPC): a state of the art review, Eng. Struct. 205 (2020) 110035.
[44] C.-C. Hung, S. El-Tawil, S.-H. Chao, A review of developments and challenges for UHPC in structural engineering: behavior, analysis, and design, J. Struct. Eng. 147 (2021) 03121001.
[45] M. Ye, L. Li, B. Pei, D.-Y. Yoo, H. Li, C. Zhou, A critical review on shear performance of joints in precast Ultra-High-Performance Concrete (UHPC) segmental bridges, Eng. Struct. 301 (2024) 117224.
[46] N. Das, P. Nanthagopalan, State-of-the-art review on ultra high performance concrete-Ballistic and blast perspective, Cement Concr. Compos. 127 (2022) 104383.
[47] Sharma H. Rizwanullah, Blast loading effects on UHPFRC structural elements: a review, Innovative Infrastructure Solutions 7 (2022) 341.
[48] E. Sammarco, C. Jones, E. Williamson, H. Sprague, Design for blast and seismic: acknowledging differences and leveraging synergies, Structure Magazine (2014) 10–14.
[49] W. Kennedy, Explosions and Explosives in Air, NDRC, Washington DC, USA, 1946.
[50] U. DoD, Structures to Resist the Effects of Accidental Explosions: UFC 3-340-02, US DoD, Washington, DC, 2008.

[51] D. Dusenberry, J. Schmidt, P. Hobelmann, Blast Protection of Buildings, ASCE/SEI 59-11, American Society of Civil Engineers, Reston, 2011.
[52] Y. Han, H. Liu, Finite element simulation of medium-range blast loading using LS-DYNA, Shock Vib. 2015 (2015).
[53] S.L. Orton, V.P. Chiarito, J.K. Minor, T.G. Coleman, Experimental testing of CFRP-strengthened reinforced concrete slab elements loaded by close-in blast, J. Struct. Eng. 140 (2014) 04013060.
[54] Q. Su, H. Wu, H. Sun, Q. Fang, Experimental and numerical studies on dynamic behavior of reinforced UHPC panel under medium-range explosions, Int. J. Impact Eng. 148 (2021) 103761.
[55] R. Jeremić, Z. Bajić, An approach to determining the TNT equivalent of high explosives, Sci. Technol. Rev. 56 (2006) 58–62.
[56] W.E. Baker, P. Cox, J. Kulesz, R. Strehlow, P. Westine, Explosion Hazards and Evaluation, Elsevier, 2012.
[57] H. Hao, Y. Hao, J. Li, W. Chen, Review of the current practices in blast-resistant analysis and design of concrete structures, Adv. Struct. Eng. 19 (2016) 1193–1223.
[58] L. Gan, Z. Zong, C. Gao, M. Li, H. Qian, Influence of shape of cuboid explosives on response of plates subjected to blast loads, Thin-Walled Struct. 174 (2022) 109077.
[59] C. Wu, G. Fattori, A. Whittaker, D.J. Oehlers, Investigation of air-blast effects from spherical-and cylindrical-shaped charges, Int. J. Prot. Struct. 1 (2010) 345–362.
[60] Y. Shi, N. Wang, J. Cui, C. Li, X. Zhang, Experimental and numerical investigation of charge shape effect on blast load induced by near-field explosions, Process Saf. Environ. Protect. 165 (2022) 266–277.
[61] J. Shin, Air-blast Effects on Civil Structures, State University of New York at Buffalo, 2014.
[62] J. Li, C. Wu, H. Hao, An experimental and numerical study of reinforced ultra-high performance concrete slabs under blast loads, Mater. Des. 82 (2015) 64–76.
[63] J. Liu, C. Wu, C. Li, W. Dong, Y. Su, J. Li, N. Cui, F. Zeng, L. Dai, Q. Meng, Blast testing of high performance geopolymer composite walls reinforced with steel wire mesh and aluminium foam, Construct. Build. Mater. 197 (2019) 533–547.
[64] U.S.A.C.E. Unified, Facilities Criteria (UFC)-Structures to Resist the Effects of Accidental Explosions (UFC 3-340-02), USACE Vicksburg, VA, 2008.
[65] J. Li, H. Hao, Numerical study of concrete spall damage to blast loads, Int. J. Impact Eng. 68 (2014) 41–55.
[66] Y. Shi, H. Hao, Z.-X. Li, Numerical derivation of pressure-impulse diagrams for prediction of RC column damage to blast loads, Int. J. Impact Eng. 35 (2008) 1213–1227.
[67] C. Zhang, G. Gholipour, A.A. Mousavi, Blast loads induced responses of RC structural members: state-of-the-art review, Compos. B Eng. 195 (2020) 108066.
[68] J. Li, H. Hao, Numerical study of structural progressive collapse using substructure technique, Eng. Struct. 52 (2013) 101–113.
[69] B.M. Luccioni, R.D. Ambrosini, R.F. Danesi, Analysis of building collapse under blast loads, Eng. Struct. 26 (2004) 63–71.
[70] J. Li, C. Wu, H. Hao, Y. Su, Z.-X. Li, A study of concrete slabs with steel wire mesh reinforcement under close-in explosive loads, Int. J. Impact Eng. 110 (2017) 242–254.
[71] J. Li, C. Wu, H. Hao, Z. Wang, Y. Su, Experimental investigation of ultra-high performance concrete slabs under contact explosions, Int. J. Impact Eng. 93 (2016) 62–75.
[72] M. Morishita, H. Tanaka, M. Ito, H. Yamaguchi, Damage of reinforced concrete slabs subjected to contact detonations, J. Struct. Eng. 46 (2000) 1787–1797.
[73] M.K. McVay, Spall Damage of Concrete Structures, ARMY Engineer Waterways Experiment Station Vicksburg MS Structures LAB, 1988.
[74] Q. Li, H. Meng, Pressure-impulse diagram for blast loads based on dimensional analysis and single-degree-of-freedom model, J. Eng. Mech. 128 (2002) 87–92.
[75] W. El-Dakhakhni, W. Mekky, S. Changiz-Rezaei, Vulnerability screening and capacity assessment of reinforced concrete columns subjected to blast, J. Perform. Constr. Facil. 23 (2009) 353–365.
[76] C.S. Association, Design and Assessment of Buildings Subjected to Blast Loads, Canadian Standards Association, 2012.
[77] G. Ma, H. Shi, D. Shu, P–I diagram method for combined failure modes of rigid-plastic beams, Int. J. Impact Eng. 34 (2007) 1081–1094.
[78] X. Hou, S. Cao, Q. Rong, W. Zheng, A PI diagram approach for predicting failure modes of RPC one-way slabs subjected to blast loading, Int. J. Impact Eng. 120 (2018) 171–184.
[79] K. Morrill, L. Malvar, J. Crawford, J. Ferritto, Blast resistant design and retrofit of reinforced concrete columns and walls. Structures 2004: building on the Past, Securing the Future (2004) 1–8.
[80] H. Draganić, D. Varevac, S. Lukić, An overview of methods for blast load testing and devices for pressure measurement, Adv. Civ. Eng. 2018 (2018) 1–20.
[81] J. Ciccarelli, A. Henderson, K. Jordans, B. Noack, D. Oehlers, C. Wu, Resistance against explosive loading of metal foam retrofitted and ultra high strength concrete structural members, Final Year Res Rep (2008).
[82] J. Xu, C. Wu, H. Xiang, Y. Su, Z.-X. Li, Q. Fang, H. Hao, Z. Liu, Y. Zhang, J. Li, Behaviour of ultra high performance fibre reinforced concrete columns subjected to blast loading, Eng. Struct. 118 (2016) 97–107.
[83] J. Yan, Y. Liu, F. Bai, X. Ni, Y. Xu, Z. Yan, F. Huang, Dynamic response of GFRP-reinforced UHPC beams under close-in blast loading, Mater. Des. 223 (2022) 111140.
[84] L. Stewart, K. Morrill, K. Natesaiyer, Development of high performance concrete panels for curtain wall systems, Structures Congress 2012 (2012) 333–344.
[85] O. Algassem, Y. Li, H. Aoude, Ability of steel fibers to enhance the shear and flexural behavior of high-strength concrete beams subjected to blast loads, Eng. Struct. 199 (2019) 109611.
[86] H. Aoude, F.P. Dagenais, R.P. Burrell, M. Saatcioglu, Behavior of ultra-high performance fiber reinforced concrete columns under blast loading, Int. J. Impact Eng. 80 (2015) 185–202.
[87] B. Ellis, B. DiPaolo, D. McDowell, M. Zhou, Experimental investigation and multiscale modeling of ultra-high-performance concrete panels subject to blast loading, Int. J. Impact Eng. 69 (2014) 95–103.
[88] C. Guertin-Normoyle, Blast Performance of Ultra-high Performance Concrete Beams Tested under Shock-Tube Induced Loads: Université D, Ottawa/University of Ottawa, 2018.
[89] A. Remennikov, B. Uy, E. Chan, D. Ritzel, The Australian National Facility for Physical Blast Simulation, 2019.
[90] E.C.J. Gan, A. Remennikov, D. Ritzel, B. Uy, Approximating a far-field blast environment in an advanced blast simulator for explosion resistance testing, Int. J. Prot. Struct. 11 (2020) 468–493.
[91] Manual L-Dkus, Livermore Software Technology Corporation, Volume I, LSTC, California, USA, 2007.
[92] ANSYS, AUTODYN User Manual Version 12.0, ANSYS, Inc., Canonsburg, PA, 2009.
[93] A.U. Manual, Abaqus user manual, Abacus (2020).
[94] M. Abedini, C. Zhang, Performance assessment of concrete and steel material models in ls-dyna for enhanced numerical simulation, a state of the art review, Arch. Comput. Methods Eng. 28 (2021) 2921–2942.
[95] J. Cui, H. Hao, Y. Shi, Discussion on the suitability of concrete constitutive models for high-rate response predictions of RC structures, Int. J. Impact Eng. 106 (2017) 202–216.
[96] J.M. Biggs, Introduction to Structural Dynamics, McGraw-Hill College, 1964.
[97] J. Jones, C. Wu, D. Oehlers, A. Whittaker, W. Sun, S. Marks, R. Coppola, Finite difference analysis of simply supported RC slabs for blast loadings, Eng. Struct. 31 (2009) 2825–2832.
[98] A.C. Jacinto, R.D. Ambrosini, R.F. Danesi, Experimental and computational analysis of plates under air blast loading, Int. J. Impact Eng. 25 (2001) 927–947.
[99] A.S.C.E. TCoB-RDotPCotEDo, Design of Blast-Resistant Buildings in Petrochemical Facilities, American Society of Civil Engineers, 2010.
[100] H. Hao, Predictions of structural response to dynamic loads of different loading rates, Int. J. Prot. Struct. 6 (2015) 585–605.
[101] T. Ngo, P. Mendis, T. Krauthammer, Behavior of ultrahigh-strength prestressed concrete panels subjected to blast loading, J. Struct. Eng. 133 (2007) 1582.
[102] L. Mao, S. Barnett, D. Begg, G. Schleyer, G. Wight, Numerical simulation of ultra high performance fibre reinforced concrete panel subjected to blast loading, Int. J. Impact Eng. 64 (2014) 91–100.
[103] V.-C. Mai, N.-Q. Vu, V.-T. Nguyen, H. Pham, Ultra-high performance fiber reinforced concrete panel subjected to severe blast loading, Defence Sci. J. 70 (2020).
[104] C. Wu, D. Oehlers, M. Rebentrost, J. Leach, A. Whittaker, Blast testing of ultra-high performance fibre and FRP-retrofitted concrete slabs, Eng. Struct. 31 (2009) 2060–2069.
[105] X. Lin, Numerical simulation of blast responses of ultra-high performance fibre reinforced concrete panels with strain-rate effect, Construct. Build. Mater. 176 (2018) 371–382.
[106] M. Foglar, R. Hajek, J. Fladr, J. Pachman, J. Stoller, Full-scale experimental testing of the blast resistance of HPFRC and UHPFRC bridge decks, Construct. Build. Mater. 145 (2017) 588–601.
[107] N.-H. Yi, J.-H.J. Kim, T.-S. Han, Y.-G. Cho, J.H. Lee, Blast-resistant characteristics of ultra-high strength concrete and reactive powder concrete, Construct. Build. Mater. 28 (2012) 694–707.
[108] L. Mao, S.J. Barnett, A. Tyas, J. Warren, G. Schleyer, S. Zaini, Response of small scale ultra high performance fibre reinforced concrete slabs to blast loading, Construct. Build. Mater. 93 (2015) 822–830.
[109] J. Dragos, C. Wu, M. Haskett, D. Oehlers, Derivation of normalized pressure impulse curves for flexural ultra high performance concrete slabs, J. Struct. Eng. 139 (6) (2013) 875–885.
[110] J. Li, C. Wu, H. Hao, Investigation of ultra-high performance concrete slab and normal strength concrete slab under contact explosion, Eng. Struct. 102 (2015) 395–408.
[111] B. Luccioni, F. Isla, R. Codina, D. Ambrosini, R. Zerbino, G. Giaccio, M.C. Torrijos, Effect of steel fibers on static and blast response of high strength concrete, Int. J. Impact Eng. 107 (2017) 23–37.
[112] W. Wan, J. Yang, G. Xu, Y. Liu, Determination and evaluation of Holmquist-Johnson-Cook constitutive model parameters for ultra-high-performance concrete with steel fibers, Int. J. Impact Eng. 156 (2021) 103966.
[113] J. Liu, J. Li, J. Fang, K. Liu, Y. Su, C. Wu, Investigation of ultra-high performance concrete slabs under contact explosions with a calibrated K&C model, Eng. Struct. 255 (2022) 113958.
[114] J. Liu, Y. Peng, S. Xu, P. Yuan, K. Qu, X. Yu, F. Hu, W. Zhang, Y. Su, Investigation of geopolymer-based ultra-high performance concrete slabs against contact explosions, Construct. Build. Mater. 315 (2022) 125727.
[115] M.K. Almustafa, M.L. Nehdi, Machine learning prediction of structural response of steel fiber-reinforced concrete beams subjected to far-field blast loading, Cement Concr. Compos. 126 (2022) 104378.
[116] J. Li, C. Wu, H. Hao, Z. Liu, Post-blast capacity of ultra-high performance concrete columns, Eng. Struct. 134 (2017) 289–302.
[117] R. Burrell, Performance of Steel Fibre Reinforced Concrete Columns under Shock Tube Induced Shock Wave Loading, University of Ottawa, Canada, 2012.

[118] S. Astarlioglu, T. Krauthammer, Response of normal-strength and ultra-high-performance fiber-reinforced concrete columns to idealized blast loads, Eng. Struct. 61 (2014) 1–12.
[119] C. Roller, C. Mayrhofer, W. Riedel, K. Thoma, Residual load capacity of exposed and hardened concrete columns under explosion loads, Eng. Struct. 55 (2013) 66–72.
[120] J. Li, C. Wu, Damage evaluation of ultra-high performance concrete columns after blast loads, Int. J. Prot. Struct. 9 (2018) 44–64.
[121] Q. Rong, Z. Zhao, X. Hou, Z. Jiang, A PI diagram approach for predicting dynamic response and damage assessment of reactive power concrete columns subjected to blast loading, Buildings 12 (2022) 462.
[122] J. Liu, C. Wu, J. Li, Y. Su, X. Chen, Numerical investigation of reactive powder concrete reinforced with steel wire mesh against high-velocity projectile penetration, Construct. Build. Mater. 166 (2018) 855–872.
[123] J. Liu, C. Wu, J. Li, Y. Su, R. Shao, Z. Liu, G. Chen, Experimental and numerical study of reactive powder concrete reinforced with steel wire mesh against projectile penetration, Int. J. Impact Eng. 109 (2017) 131–149.
[124] J. Li, C. Wu, H. Hao, Y. Su, Experimental and numerical study on steel wire mesh reinforced concrete slab under contact explosion, Mater. Des. 116 (2017) 77–91.
[125] D. Zhu, S. Liu, Y. Yao, G. Li, Y. Du, C. Shi, Effects of short fiber and pre-tension on the tensile behavior of basalt textile reinforced concrete, Cement Concr. Compos. 96 (2019) 33–45.
[126] N. Williams Portal, K. Lundgren, H. Wallbaum, K. Malaga, Sustainable potential of textile-reinforced concrete, J. Mater. Civ. Eng. 27 (2015) 04014207.
[127] J. Jiang, C. Jiang, B. Li, P. Feng, Bond behavior of basalt textile meshes in ultra-high ductility cementitious composites, Compos. B Eng. 174 (2019) 107022.
[128] J. Liu, C. Liu, S. Xu, J. Li, J. Fang, Y. Su, C. Wu, G-UHPC slabs strengthened with high toughness and lightweight energy absorption materials under contact explosions, J. Build. Eng. 50 (2022) 104138.
[129] L.-H. Han, W. Li, R. Bjorhovde, Developments and advanced applications of concrete-filled steel tubular (CFST) structures: members, J. Constr. Steel Res. 100 (2014) 211–228.
[130] P. Ayough, N.R. Sulong, Z. Ibrahim, Analysis and review of concrete-filled double skin steel tubes under compression, Thin-Walled Struct. 148 (2020) 106495.
[131] H. Wu, Y. Peng, Q. Fang, Experimental and numerical study of ultra-high performance cementitious composites filled steel tube (UHPCC-FST) subjected to close-range explosion, Int. J. Impact Eng. 141 (2020) 103569.
[132] Q. Su, H. Wu, L. Poh, F. Zhang, F. Zhou, S. Pang, Dynamic behavior of UHPC-FST under close-in explosions with large charge weight, Eng. Struct. 277 (2023) 115475.
[133] Z. Wang, H. Wu, J. Wu, Q. Fang, Experimental study on the residual seismic resistance of ultra high performance cementitious composite filled steel tube (UHPCC-FST) after contact explosion, Thin-Walled Struct. 154 (2020) 106852.
[134] Z. Wang, H. Wu, Q. Fang, J. Wu, Numerical study on the residual axial capacity of ultra high performance cementitious composite filled steel tube (UHPCC-FST) column under contact explosion, Thin-Walled Struct. 153 (2020) 106832.
[135] F. Zhang, C. Wu, X.-L. Zhao, H. Xiang, Z.-X. Li, Q. Fang, Z. Liu, Y. Zhang, A. Heidarpour, J.A. Packer, Experimental study of CFDST columns infilled with UHPC under close-range blast loading, Int. J. Impact Eng. 93 (2016) 184–195.
[136] F. Zhang, C. Wu, X.-L. Zhao, A. Heidarpour, Z. Li, Experimental and numerical study of blast resistance of square CFDST columns with steel-fibre reinforced concrete, Eng. Struct. 149 (2017) 50–63.
[137] A. Lampropoulos, S.A. Paschalis, O. Tsioulou, S.E. Dritsos, Strengthening of reinforced concrete beams using ultra high performance fibre reinforced concrete (UHPFRC), Eng. Struct. 106 (2016) 370–384.
[138] J. Liu, Z. He, P. Liu, J. Wei, J. Li, C. Wu, High-velocity projectile impact resistance of reinforced concrete slabs with ultra-high performance concrete strengthening-A numerical study, Structures 52 (2023) 422–436.
[139] J. Wei, J. Li, C. Wu, H. Hao, J. Liu, Experimental and numerical study on the impact resistance of ultra-high performance concrete strengthened RC beams, Eng. Struct. 277 (2023) 115474.
[140] S.A. Paschalis, A.P. Lampropoulos, O. Tsioulou, Experimental and numerical study of the performance of ultra high performance fiber reinforced concrete for the flexural strengthening of full scale reinforced concrete members, Construct. Build. Mater. 186 (2018) 351–366.
[141] H. Yin, W. Teo, K. Shirai, Experimental investigation on the behaviour of reinforced concrete slabs strengthened with ultra-high performance concrete, Construct. Build. Mater. 155 (2017) 463–474.
[142] T. Noshiravani, E. Brühwiler, Experimental investigation on reinforced ultra-high-performance fiber-reinforced concrete composite beams subjected to combined bending and shear, ACI Struct. J. 110 (2013) 251–261.
[143] C. Li, H. Aoude, Effect of UHPC jacketing on the shear and flexural behaviour of high-strength concrete beams, Structures 51 (2023) 1972–1996.
[144] M. Safdar, T. Matsumoto, K. Kakuma, Flexural behavior of reinforced concrete beams repaired with ultra-high performance fiber reinforced concrete (UHPFRC), Compos. Struct. 157 (2016) 448–460.
[145] A. Gholampour, R. Hassanli, J.E. Mills, T. Vincent, M. Kunieda, Experimental investigation of the performance of concrete columns strengthened with fiber reinforced concrete jacket, Construct. Build. Mater. 194 (2019) 51–61.
[146] J. Li, J. Gong, L. Wang, Seismic behavior of corrosion-damaged reinforced concrete columns strengthened using combined carbon fiber-reinforced polymer and steel jacket, Construct. Build. Mater. 23 (2009) 2653–2663.
[147] J.P. Firmo, J.R. Correia, L.A. Bisby, Fire behaviour of FRP-strengthened reinforced concrete structural elements: a state-of-the-art review, Compos. B Eng. 80 (2015) 198–216.
[148] G. Ma, G. Bai, L. Wang, F. Wang, Explosion resistance of 3D printing ultra-high performance concrete based on contact explosion tests, Int. J. Impact Eng. 169 (2022) 104316.
[149] C. Li, H. Aoude, Influence of UHPFRC jacketing on the static, blast and post-blast behaviour of doubly-reinforced concrete beams, Int. J. Impact Eng. 179 (2023) 104656.
[150] C. Li, H. Aoude, Behaviour of UHPFRC-retrofitted RC beams with varying strengthening configurations under single and repeated blast loading, Cement Concr. Compos. (2023) 105180.
[151] J.-Y. Lee, H. Aoude, Y.-S. Yoon, D. Mitchell, Impact and blast behavior of seismically-detailed RC and UHPFRC-Strengthened columns, Int. J. Impact Eng. 143 (2020) 103628.
[152] J. Wang, W. Yuan, R. Feng, J. Guo, X. Dang, Dynamic performances of ultra-high-performance fiber-reinforced concrete-strengthened concrete columns subjected to blast impacts, Adv. Struct. Eng. 23 (2020) 3009–3023.
[153] S. El-Tawil, Y.-S. Tai, J.A. Belcher II, D. Rogers, Open-recipe ultra-high-performance concrete, Concr. Int. 42 (2020) 33–38.
[154] G.K. Schleyer, S. Barnett, S. Millard, M. Rebentrost, G. Wight, UHPFRC Panel Testing, 2011.
[155] Q. Su, H. Wu, Q. Fang, Calibration of KCC model for UHPC under impact and blast loadings, Cement Concr. Compos. 127 (2022) 104401.
[156] J. Kim, N. Yi, I. Oh, H. Lee, J. Choi, Y. Cho, Blast loading response of ultra high performance concrete and reactive powder concrete slabs, Proceedings of Fracture Mechanics of Concrete and Concrete Structures (2010) 1715–1722.
[157] Y. Peng, C. Wu, J. Li, J. Liu, X. Liang, Mesoscale analysis on ultra-high performance steel fibre reinforced concrete slabs under contact explosions, Compos. Struct. 228 (2019) 111322.
[158] J. Li, C. Wu, H. Hao, Y. Su, Investigation of ultra-high performance concrete under static and blast loads, Int. J. Prot. Struct. (2015).